Nuclear Materials and Energy 42 (2025) 101854

Contents lists available at ScienceDirect

Nuclear Materials and Energy

journal homepage: www.elsevier.com/locate/nme

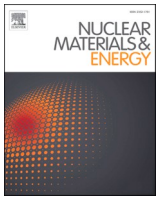

Plasma-wall interaction impact of the ITER re-baseline☆

R.A. Pitts [a,*], A. Loarte [a], T. Wauters [a], M. Dubrov [a], Y. Gribov [a], F. Köchl [a], A. Pshenov [a], Y. Zhang [b], J. Artola [a], X. Bonnin [a], L. Chen [a], M. Lehnen [a,2], K. Schmid [c,1], R. Ding [d,1], H. Frerichs [e,1], R. Futtersack [f], X. Gong [d], G. Hagelaar [g], E. Hodille [h,1], J. Hobirk [c], S. Krat [i,1], D. Matveev [j,1], K. Paschalidis [k], J. Qian [d], S. Ratynskaia [k], T. Rizzi [k], V. Rozhansky [l,1], P. Tamain [h,1], P. Tolias [k], L. Zhang [d], W. Zhang [d,1]

[a] ITER Organization, Route de Vinon-sur-Verdon, CS 90 046 13067, St. Paul Lez Durance Cedex, France
[b] Key Laboratory of Materials Modification by Laser, Ion and Electron Beams (Ministry of Education), School of Physics, Dalian University of Technology, Dalian 116024, China
[c] Max-Planck-Institut für Plasmaphysik, 85748, Garching, Germany
[d] Institute of Plasma Physics, Chinese Academy of Sciences, Hefei, Anhui, China
[e] Department of Engineering Physics, University of Wisconsin, Madison, WI 53706, USA
[f] CCFE, Culham Science Centre, Abingdon OX14 3DB, UK
[g] LAPLACE, Université de Toulouse, CNRS, INPT, UPS, 118 Route de Narbonne 31062, Toulouse, France
[h] CEA, IRFM, F-13108, Saint Paul-lez-Durance, France
[i] National Research Nuclear University MEPhI, Kashirskoe Shosse, 31, Moscow, Russia
[j] Forschungszentrum Jülich GmbH, Institut fuer Energie und Klimaforschung, Jülich, Germany
[k] Space and Plasma Physics—KTH Royal Institute of Technology, Teknikringen 31 10044, Stockholm, Sweden
[l] Peter the Great St.Petersburg Polytechnic University, Polytechnicheskaya 29 195251, St.Petersburg, Russia

ARTICLE INFO

Keywords:
Tungsten
First Wall
Boronization
Limiter start-up
SOLPS-ITER
Runaway electrons

ABSTRACT

To mitigate the impact of technical delays, provide a more rationalized approach to the safety demonstration and move forward as rapidly as possible to a reactor relevant materials choice, the ITER Organization embarked in 2023 on a significant re-baselining exercise. Central to this strategy is the elimination of beryllium (Be) first wall (FW) armour in favour of tungsten (W), placing plasma-wall interaction (PWI) centre stage of this new proposal. The switch to W comes with a modified Research Plan in which a first "Start of Research Operation" (SRO) campaign will use an inertially cooled, temporary FW, allowing experience to be gained with disruption mitigation without risking damage to the complex water-cooled panels to be installed for later DT operation. Conservative assessments of the W wall source, coupled with integrated modelling of W pedestal and core transport, demonstrate that the elimination of Be presents only a low risk to the achievement of the principal ITER Q = 10 DT burning plasma target. Primarily to reduce oxygen contamination in the limiter start-up phase, known to be a potential issue for current ramp-up on W surfaces, a conventional diborane-based glow discharge boronization system is included in the re-baseline. First-of-a-kind modelling of the boronization glow is used to provide the physics specification for this system. Erosion simulations accounting for the 3D wall geometry provide estimates both of the lifetime of boron (B) wall coatings and the subsequent B migration to remote areas, providing support to a simple evaluation which concludes that boronization, if it were to be used frequently, would dominate fuel retention in an all-W ITER. Boundary plasma (SOLPS-ITER) and integrated core–edge (JINTRAC) simulations, including W erosion and transport, clearly indicate the tendency for a self-regulating W sputter source in limiter configurations and highlight the importance of on-axis electron cyclotron power deposition to prevent W core accumulation in the early current ramp phase. These predicted trends are found experimentally in dedicated W limiter start-up experiments on the EAST tokamak. The SOLPS-ITER runs are used to formulate W source boundary conditions for 1.5D DINA code scenario design simulations which demonstrate that flattop durations

☆ This article is part of a special issue entitled: 'PSI-26' published in Nuclear Materials and Energy.

* Corresponding author.
E-mail address: richard.pitts@iter.org (R.A. Pitts).

[1] Member of the ITER Scientist Fellowship Network.

[2] Deceased.

https://doi.org/10.1016/j.nme.2024.101854
Received 31 July 2024; Received in revised form 19 December 2024; Accepted 19 December 2024
Available online 28 December 2024

of ~100 s should be possible in hydrogen L-modes at nominal field and current (I_p = 15 MA, B_T = 5.3 T) which are one of the principal SRO targets. Runaway electrons (RE) are considered to be a key threat to the integrity of the final, actively cooled FW panels. New simulations of RE deposition and subsequent thermal transport in W under conservative assumptions for the impact energy and spatial distribution, conclude that there is a strong argument to increase the W armour thickness in key FW areas to improve margins against cooling channel interface damage in the early DT operation phases when new RE seeds will be experienced for the first time.

1. Introduction

The ITER Organization (IO) began in early 2023 an exercise of re-baselining in which a key element is the change of first wall (FW) material from beryllium (Be) to tungsten (W). Given the much higher energy threshold (> factor 10 for deuterium (D) on W cf. D on Be) and lower yield (<10^3 for D on W cf. D on Be for low energies) for W physical sputtering, together with a much higher melting point ($T_{melt,W}$ = 3422°C cf. $T_{melt,Be}$ = 1287°C), switching from Be to W FW armour has clear positive benefits in terms of wall armour erosion lifetime, the associated tritium (T) fuel retention by co-deposition, dust production and resilience to disruption thermal loads during unmitigated or partially mitigated disruptions. Substituting Be with W also avoids the well-known issues of Be handling during assembly/disassembly and eliminates the need for the extremely complex and costly replacement of an actively cooled FW that would be required later in the project lifecycle if ITER is to be a true testbed for fusion reactor relevant main chamber armour material. This said, the re-baseline does, in fact, include a FW replacement, but not the exchange of one actively cooled system for another. Operation will instead begin with a temporary, inertially cooled FW, allowing experience to be gained with disruptions and their mitigation (particularly the difficult issue of runaway electrons (RE)) without risking damage to the final panels to be installed for DT operation.

Despite the advantages of W over Be, increasing the W plasma-facing surface by an additional ~600 m^2 (compared with the existing ~140 m^2 of W armour in the divertor) comes with the obvious risk of higher levels of core plasma W content, leading in turn to radiative losses which may prevent sustainment of H-mode and hence directly impact the achievement of the principal ITER high Q objective. Plasma current ramp-up, which on ITER will be performed in limiter configuration on the high field side (HFS) blanket FW [1], is also likely to be more challenging than with Be plasma-facing components (PFC) due to the much stronger line radiation from W. This start-up problem is exacerbated by the removal of Be which has excellent impurity gettering properties, particularly for oxygen (O), which may act as a seed for W sputtering during the limiter phase. Present full-W devices thus often find that depositing a thin boron (B) coating on PFCs through the technique of glow discharge plasma-assisted chemical vapour deposition (boronization) provides for easier plasma initiation and start-up, though in ITER this comes with the caveat of increased fuel (T) retention by co-deposition with the eroded B. As a risk mitigation measure, the re-baseline includes the design and installation of a conventional boronization system on ITER.

Compared to the situation when the ITER machine was first being designed, and even at the formal establishment of the IO in October 2007, far more is known today regarding tokamak operation with W PFCs. Several research devices (e.g. ASDEX Upgrade [2], WEST [3], EAST [4], C-Mod [5] (before it was definitively shutdown in 2016)) have routine experience of operating with high Z (W and molybdenum (Mo)) main wall armour. Others (e.g. KSTAR [6], which has recently installed an actively cooled, ITER-like divertor) will soon make the transition to full W, or are under construction with full W armour planned from the start (e.g. COMPASS-U [7], DTT [8], SPARC [9]). The result is that a move to a full-W ITER today is associated with far lower risk to the key mission goals than would have been the case had the decision been taken many years earlier. Careful assessment is nevertheless required of the physics and operational issues an all-W ITER will face and many naturally fall squarely within the domain of plasma-wall interaction (PWI). Any such assessments are of course associated with (often considerable) uncertainty, particularly with regard to the question of how an additional W wall source may affect the achievement of the principal Q = 10 objective. As always in making ITER performance projections, a conservative approach is adopted, taking worst case assumptions. For example, it will be demonstrated that Q = 10 operation should be achievable even if the integral wall W source exceeds what is presently considered to be plausible worst case far scrape-off layer (SOL) conditions.

It is the intention of this paper to summarize the significant PWI physics analysis in support of the re-baseline which has been undertaken by the ITER Organization, together with collaborators from the plasma boundary community within the ITER member institutions, including the ITER Scientist Fellow Network and the International Tokamak Physics Activity. In each of the key PWI areas highlighted, it also endeavours to identify important elements of further R&D which are required to consolidate the re-baseline in the remaining years before the start of commissioning and operation. The following sections will thus discuss, in order, the issues of W main wall erosion impact on high Q performance, boronization, B layer lifetime, associated fuel retention and recovery, limiter start-up on W and unmitigated disruption transient impact on W, particularly current quench (CQ) thermal plasma loads and RE impact.

2. Revised ITER research plan

As illustrated in very brief schematic form in Fig. 1, the switch to W comes with a modified ITER Research Plan (IRP) [10,11] in which the first phase of machine exploitation, the “Start of Research Operation” (SRO), combines the previous 2016 “Staged Approach” First Plasma and non-active (hydrogen (H) and helium (He)) campaigns (referred to as Pre-Fusion Power Operation, PFPO-1 and 2) [12]. Unlike in the 2016 plan, plasma operation in the re-baseline begins with the final W divertor [13] fully installed and actively cooled. Meanwhile, the Blanket shield blocks, armoured with provisional W FW panels, are also in place, but will not be actively cooled. The principal rationale for this temporary FW (TFW) is to allow all control and protection systems to be fully commissioned up to the nominal plasma current and toroidal field, including demonstration of reliable disruption mitigation, before the very costly (and final) actively cooled FW panels are installed. In particular, due to the high plasma current, unmitigated RE impact on ITER can be potentially extremely damaging to PFCs (Section 6). Having a FW much more forgiving to transient impact in the early phase of ITER operation when the experience of avoidance and mitigation must be developed is a major advantage.

With doubled electron cyclotron (EC) heating power (40 MW up from the original 20 MW) and up to 10 MW of ion cyclotron (IC) heating available from the start of operation, SRO introduces two new and extremely advantageous features in comparison to the 2016 baseline. First, it allows ion cyclotron wall conditioning (ICWC) for fuel recovery by isotopic exchange to be demonstrated and the compatibility of RF heating with a W wall to be studied earlier, permitting decisions to be made regarding an upgrade of IC power (from a single antenna) to the original 20 MW baseline in time for DT operation. Second, it includes a short H-mode campaign in D at half nominal B_T and low I_p (2.65 T, 5–7.5 MA), enabled by the increased EC heating which provides power

sufficient to be well above the H-mode threshold in this range of current and field. This eliminates the need for the pure He plasmas planned in the original PFPO campaigns as a way to achieve first H-modes at low power (benefitting from the expected lower L-H power transition threshold in He in comparison with hydrogen (H) fuel). Although this mini-H-mode campaign will feature extremely low neutron fluence (1.5 x 10^{20}, 5x10^{-8} of the total ITER lifetime fluence) and negligible T production, it will still mark the beginning of nuclear operation on ITER. It will permit a first look at D H-modes in ITER under conditions in which uncontrolled edge localized mode (ELM) transients are not expected to damage the W divertor, and hopefully make initial tests of ELM control using the in-vessel ELM control coils. A third key deliverable of SRO is the achievement of L-mode operation in H up to the nominal field and current (5.3 T, 15 MA) – see Section 5.1 – requiring that disruption heat and electromagnetic load validation has been completed at lower I_p and that the Disruption Mitigation System (DMS) is fully operational.

To mitigate the risks posed by a W main wall for reliable plasma start-up (see Section 5), the re-baseline includes the installation of a conventional diborane (B_2H_6 or B_2D_6) boronization system (Section 4.1). The SRO phase will be the first opportunity to assess the efficacy of this system in terms of impact on plasma operation, fuel retention and B layer lifetime.

During the post-SRO Assembly phase, prior to DT operation, the TFW panels will be replaced by the final, actively cooled units and 33 MW of Neutral Beam Injection (NBI) heating will be installed along with an additional 20–27 MW of EC power (providing sufficient central and off-axis injection for heating and neoclassical tearing mode control in the DT phases). If SRO tests are successful, the IC power may also be increased by an additional 10 MW.

Operation in DT, constituting the vast majority of ITER exploitation, is split into two distinct blocks, DT-1 and 2, of which the first, limited to a neutron fluence of ~3 x 10^{25}n (1 % of the lifetime fluence) and broken down into 5 Fusion Power Operation (FPO) campaigns, has as principal objective to achieve the first Project goal of 500 MW of fusion power production with $Q \geq 10$ for $t_{burn} > 300$ s. A successful DT-1 phase will thus demonstrate that ITER can achieve DT plasmas with dominant alpha heating and that all the required scenario integration and plasma control can be maintained over timescales of hundreds of seconds. It also marks the first phase of the nuclear safety demonstration for ITER operation. In DT-2, an additional heating beam may be installed for a total $P_{NBI} = 50$ MW and the principal objectives are routine, high duty operation at $P_{fus} = 500$ MW, $Q \geq 10$ for $t_{burn} > 500$ s, routine operation at $Q \geq 5$ for $t_{burn} = 1000$ s in long pulse scenarios, and $Q \geq 5$ for $t_{burn} >$ 3000 s in steady-state, non-inductive discharges.

3. Tungsten wall impact on Q = 10

As already highlighted in Section 1, the fundamental physics and operational question to be addressed when considering a move to a full W ITER is that of core plasma W contamination. This is actually a rather complex issue, made more difficult by the fact that, due to the peculiarities of W transport, direct empirical extrapolation of the observations in current devices operating with majority W PFCs is not straightforward. Only a brief summary of the key points is provided here. More details may be found in [10,11] and references therein. Regarding first guidance from present experiments, the following points are of note:

- Stationary H-mode conditions can be maintained if the edge power flow is above some margin: $P_{sep} \gtrsim 1.5P_{LH}$, where P_{sep} and P_{LH} are respectively the powers crossing the separatrix and the H-mode transition threshold power [2 14 15]. These conditions are typically associated with core radiated power fractions of $f_{rad,core} = P_{rad,core}/P_{in} \lesssim (0.4 – 0.5)$, with P_{in} the heating power.
- Central (wave) heating (ECH, ICH) can be used to suppress uncontrolled W core accumulation [16 17], which in present machines, usually with a strong core particle source (provided by NBI), tends to be dominated by neoclassical (inwards) transport.
- ELMs play a critical role in determining the edge W source: depending on separatrix-wall gaps, they can dominate the W wall source and their frequency must be maintained at a sufficient level to ensure adequate W exhaust ("ELM flushing") [18].
- Even though the W wall source is typically only 10–20 % of the divertor source (and generally larger on the low field side (LFS) than the HFS for similar separatrix-wall gaps [19]), screening of the source is much less effective due to the much lower level of prompt re-deposition in the main SOL compared with that at the divertor targets. It can thus provide a core W source of similar strength to that originating from the divertor (for Type I ELMing discharges) [20].

Turning to the situation on ITER, the lack of any significant core particle source and the low toroidal rotation Mach number leads to the expectation from modelling that, in contrast to present devices, anomalous W transport should dominate over neoclassical inward convection in the burning plasma core [21]. In the pedestal, although uncertainties remain, gradients of temperature (strong) and density (moderate), should lead to strong neoclassical edge temperature screening such that W transport in between ELMs is outward, opposite to the behaviour found in the majority of current tokamaks [22]. Moreover, simulations predict that the ELM flushing W exhaust mechanism cited earlier is expected to invert under conditions of strong W screening in which W density profiles in the pedestal are hollow [18,23]. In this case, ELMs

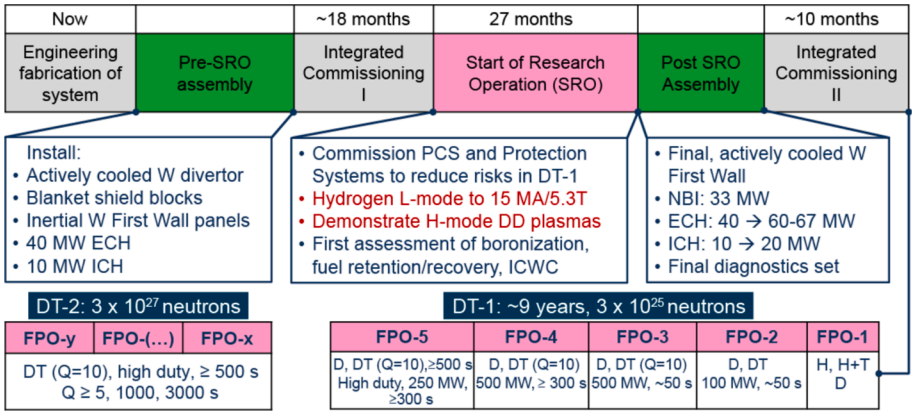

Fig. 1. Diagrammatic summary of the revised IRP accompanying the proposed re-baseline. Some of the key systems and milestones are listed explicitly for the pre- and post-assembly phases and for SRO operation itself.

would actually drive higher core W concentrations instead of flushing the W out. Thus, W density control through ELM frequency control seems unlikely to be option on ITER under burning plasma conditions and ELM control must in fact be ELM suppression [10]. This is perfectly consistent with the fact that ELMs must on ITER be kept to very low amplitudes from the point of view of W divertor monoblock lifetime (cracking, edge and front surface melting) [13]. Regarding ELM control, ITER will be equipped with an extensive set of 27 magnetic perturbation coils for the application of 3D fields [24]. Recent JOREK code modelling including a Monte Carlo particle tracker to follow W ions has demonstrated that the formation of 3D structures in the edge magnetic and electric fields promotes outward W transport in plasma conditions in which neoclassical transport in 2D would be inwards [25]. The implication is that a balance will need to be sought between the needs for ELM control and the preservation of W pedestal screening in order to minimize ITER H-mode core plasma contamination.

With all the above in mind, the impact of a W wall source on ITER high Q operation has been quantified using JINTRAC [26] core–edge-SOL integrated simulations which include core turbulent transport determined by the EDWM model [27], NEO code [28] calculations of the neoclassical W transport and the EDGE2D-EIRENE boundary plasma code. ELMs are assumed suppressed by employing the so-called continuous ELM model in which the pedestal transport coefficients are adjusted to obtain the values of pressure expected from ideal MHD modelling. In this case, the (stationary) W wall source can be generated only by the impact of plasma ion flux (fuel and impurity ions) and charge-exchange neutral (CXN) fluxes (dominated by fuel neutrals). However, since the JINTRAC computational grid does not extend beyond the first field line which intercepts the wall starting from the divertor region, it cannot self-consistently include a proper description of the plasma-main chamber wall interactions which are key to the overall Q = 10 impact assessment. These are instead modelled using the 2D WallDYN approach [29] to compute the wall W erosion flux (assuming pure W surfaces) and the W density, n_W distribution at the location of the JINTRAC outer simulation boundary (WallDYN3D calculations have been separately performed to explore B-layer lifetimes in a boronized ITER – see Section 4.2).

An effective "gas puff W wall source" is then introduced in JINTRAC and varied so as to obtain the similar values of the WallDYN W density at the computational grid edge for a range of assumptions regarding the far-SOL plasma background. For conservatism, prompt redeposition of W at the divertor targets (both for wall injected W, or W produced at the divertor) is assumed to be zero in the EDGE2D-EIRENE simulations.

As described in detail in [30], the WallDYN wall erosion calculations are very sensitive to the assumed far-SOL plasma background (predictions of which are still extremely uncertain for ITER – see below). A range of these backgrounds has been generated using the SOLPS/OSM (Onion Skin Model) approach for Q = 10 plasma conditions (used to establish the SOLPS main SOL and divertor plasma simulations which originate from [31], namely P_{SOL} = 100 MW, neon (Ne) seeding for divertor target load control, with varying assumptions for the magnitude of far-SOL radial transport and parallel flow Mach Number (M)). They determine the ion and electron temperatures, T_i, T_e, D fuel ion and CXN fluxes, charge state resolved Ne ion fluxes and averaged CXN energies at the walls, from which DIVIMP trace impurity transport simulations are used to determine the WallDYN migration matrix.

Two examples of the outer midplane (OMP) T_e and n_e radial profiles from the plasma background scan are shown in Fig. 2a (corresponding to cases 00 g and 00 m in [30], representing the extremes of high $n_{e,wall}$ and low $T_{e,wall}$ (10 eV) and low $n_{e,wall}$, high $T_{e,wall}$ (20 eV)). Both have M = 0 (stagnant SOL flow) and $T_i = 2 \times T_e$ fixed in the OSM part of the solution. A zero flow SOL is the most conservative assumption in terms of W erosion since, in this case, the eroded W accumulates at the stagnation point (near the OMP) where radial transport in the hotter regions near the separatrix allows W to charge to comparatively high states (e.g. $\sim W^{10+}$) and be much more effective for self-sputtering at the wall. Of

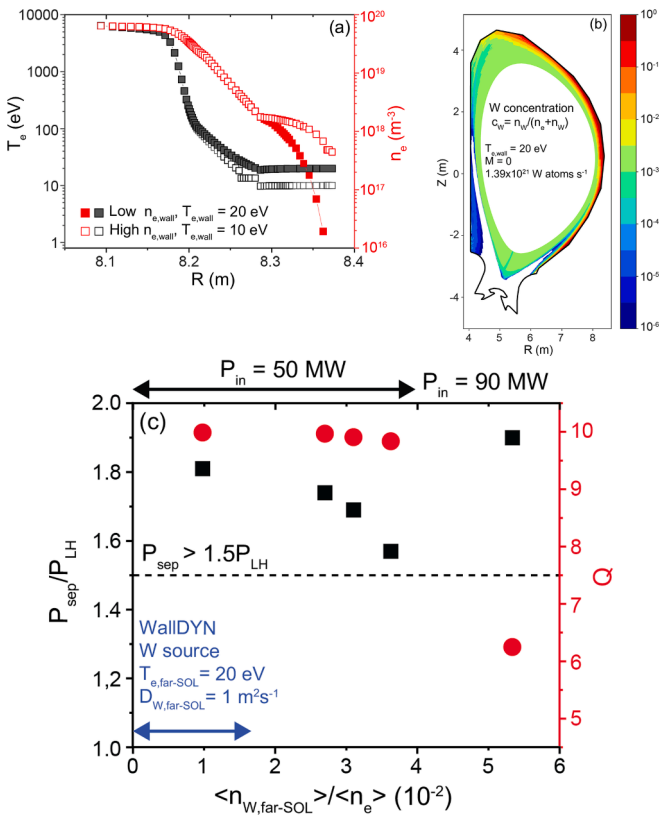

Fig. 2. Compilation describing the impact assessment of a W main chamber wall on ITER burning plasma performance: (a) examples of two extremes of OMP far-SOL n_e and T_e radial profiles resulting from OSM simulations on a grid extended to the main chamber wall; (b) WallDYN2D poloidal distribution of the W concentration for the low $n_{e,wall}$, high $T_{e,wall}$ stagnant SOL flow plasma background case (OSM run "00 g") – this yields the highest W influx of all available plasma backgrounds in the OSM database; (c) JINTRAC predictions for the dependence of Q and the ratio of power crossing the separatrix to the H-mode threshold power on the normalized W density from WallDYN.

the two examples in Fig. 2a, the high $T_{e,wall}$, $T_{i,wall}$ condition yields a total W source of ~1.4 x 10^{21} atoms s^{-1}, the worst case in the entire database. Fig. 2b shows the corresponding 2D distribution of W concentration (expressed as $n_W/(n_e + n_W)$ which is essentially a plasma density fraction since $n_W \ll n_e$, except in the very far SOL where n_e is very low and $n_W \sim 0.1 n_e$).

Analysis of the WallDYN results demonstrates unequivocally that the W erosion source is dominated by Ne and W self-sputtering, with negligible W release by D CXN impact. Thus, the use of impurity for divertor power flux control is ultimately the strongest driver for the W wall source since it is the Ne seed which produces the primary erosion, thereafter augmented by W self-sputtering. This an interesting contrast to the situation with Be, where D CXN sputtering contributes a much larger fraction of the wall impurity release due to the lower sputtering threshold and higher yield of D → Be [32]. Of note also is that in the WallDYN workflow, DIVIMP account for prompt re-deposition of eroded W and finds very low re-deposition fractions (~10 %) at the main chamber walls, consistent with the experimental findings mentioned earlier and confirming the very poor screening (due to the lower plasma densities) compared with the divertor source.

Fig. 2c summarises the outcome of the JINTRAC simulations using the WallDYN effective W sources in terms of the dependence of the fusion power gain (Q) on $n_{W,far\text{-}SOL}$, the W density at the JINTRAC outer computational boundary (normalized to the volume averaged electron density, $\langle n_e \rangle$). It demonstrates that Q = 10 performance (P_{in} = 50 MW at I_p = 15 MA, B_T = 5.3 T) can be maintained up to the worst case

WallDYN W influxes in ITER baseline H-modes with standard H-mode confinement (noting again the very conservative assumption in JINTRAC of zero prompt re-deposition for W evolved at the divertor). For even higher $n_{W,far\text{-}SOL}$, corresponding to W influxes ~3x above those corresponding to the most conservative WallDYN source, higher P_{in} (90 MW) is required to compensate the increased core radiation (~70 MW, of which ~50 MW due to W) and maintain the edge power flow above the L-H transition threshold. In this case Q falls to lower values (~6 in Fig. 2c). On the basis of these JINTRAC integrated modelling estimates, it may thus be concluded that the risk to Q = 10 performance of switching to a full-W main wall on ITER is rather low.

This important conclusion notwithstanding, it is worth emphasizing once more the significance of the far-SOL plasma in this analysis. Despite decades of tokamak research, and an accepted understanding that the far-SOL plasma parameters are driven mostly by turbulent filaments, predictive capability for this tenuous region at the ITER scale under burning conditions remains elusive. Although there is some experimental justification from present, smaller devices for the worst case far-SOL plasma parameter assumptions in the WallDYN W source calculations for ITER, there is still no theoretical basis on which to decide the radial structure of the far-SOL profiles of temperature and density. Will the profiles have broad shoulders as usually seen in present experiments under H-mode conditions at high density (see e.g. [33], though H-mode data are sparse)? Will $T_{e,wall}$, $T_{i,wall}$ at the main chamber walls be as high as the worst case ITER assumptions? Is there a clear link to the upstream profile structure and the divertor detachment state at the ITER scale? Until these questions are answered, there will always be large uncertainties in the types of assessment described above in the context of a W main wall source. The same applies to the wide range of studies that have been previously performed for ITER regarding erosion, material migration and fuel retention by co-deposition with Be main chamber armour (see e.g. [32,34,35,36].

In the meantime, whilst this does not resolve the underlying problem, IO has been pushing over recent years a concerted effort to improve at the least the consistency of plasma boundary modelling in the sense of providing simulations with numerical grids right up to all main chamber wall surfaces. This avoids the need for the SOLPS/OSM patch used in the WallDYN approach and instead the far-SOL is self-consistently treated in the boundary codes, although the magnitude and radial variation of the cross-field anomalous transport must still be specified across the simulation domain. Fig. 3 illustrates how three of the Fusion Community's main plasma boundary simulation codes, SOLPS-ITER, SOLEDGE3X-EIRENE and EMC3-EIRENE are now at the stage at which extended numerical grids are established for exactly the same ITER magnetic equilibrium, taken from a DINA code simulation stored in ITER's Integrated Modelling Analysis Suite (IMAS), corresponding to a point roughly in the middle of the flattop of a standard 15 MA burning plasma (Q = 10) scenario. All three codes use the EIRENE kinetic neutral Monte Carlo code [37].

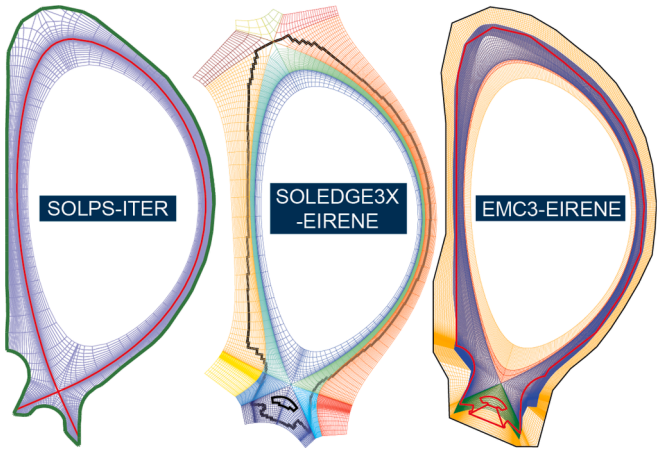

Fig. 3. Numerical grids extending to all main chamber walls are now available and in use for three leading plasma boundary simulation tools. All three ITER grids in this example are generated from the same magnetic equilibrium extracted at timeslice 399 of the DINA IMAS database shot 135011, run 7.

In the case of SOLPS-ITER [38,39], considerable enhancements, conducted over a multi-year development programme, have been necessary to make this possible [40] and first simulations at the ITER scale are only just beginning at the time of writing. For SOLEDGE3X, a more modern code in which wide grids are a built-in feature [41], many code runs are already available (in IMAS) for low power ITER cases [42] and the first burning plasma runs have started to appear [43]. Regarding EMC3-EIRENE, wide grids have previously been used assuming toroidal symmetry for the main wall [44], but the new grid example shown in Fig. 3 includes, the full 3D wall shaping and is particularly important for the assessments of B layer lifetime discussed in Section 4.2, where, unlike the case of pure W, erosion of the coating in plasma recessed areas by CXN fluxes is a key factor as a result of the lower B sputter threshold and higher yield (similar to the case of Be walls). For more realistic coating lifetime and B migration estimates, it is thus important to include the 3D wall shape to properly account for the different erosion rates of plasma wetted and recessed zones.

One final point to make concerning these plasma backgrounds is that the more modern extended grids in Fig. 3 properly account both for the most recent ITER first wall contour and the most up-to-date magnetic equilibrium foreseen for burning plasma operation. Compared with the older grids, using which the W main wall fusion performance impact study summarized in Fig. 2c was performed, the new equilibrium has lower OMP primary to secondary separatrix separation, d_{rsep} ~6.5 cm (cf. ~9 cm in the older equilibrium) and greater clearance to the inner wall. The net result is a considerably lower plasma-wall interaction, particularly in the upper HFS wall regions. As a consequence, the W erosion simulations described above, as well as the many previous erosion-migration studies which have been performed in past years for ITER [32,34,35,36], are conservative with respect to total erosion. Going forward beyond the initial simulation studies in support of the re-baseline physics case described here, all future erosion/migration assessments should by default use the new plasma backgrounds which are being generated on the updated wide grids.

4. Boronization, fuel retention and recovery

Apart from the obvious benefit of offering a low Z material facing the plasma in the main chamber, Be has the very useful property of being an excellent O getter, forming a stable oxide. As demonstrated very clearly by the JET experience with the ITER-Like Wall, plasma breakdown/start-up with large scale Be coverage, particularly after long maintenance periods with vacuum vessel venting, is much easier in comparison even with carbon PFCs [45]. Replacing Be with W means not only that the O gettering action is lost, but that limiter start-up on W PFCs can be potentially more difficult if there are too high levels of low-medium Z impurities in the early current ramp-up phase. They may act both as contributors to plasma radiation losses and as seeds for W sputtering, which in turn further increases the radiation loss.

As a risk mitigation measure, particularly for potential plasma start-up issues, the ITER re-baseline includes a standard diborane glow discharge boronization system, of the type installed on many of the world's research tokamaks. The thin (typically 50–100 nm thick), amorphous B layers which cover PFC surfaces following boronization are ephemeral on strongly plasma wetted areas, but have much longer lifetime in recessed zones and are demonstrably routinely effective in current full-W devices at removing intrinsic O contamination for hundreds of plasma discharges following a coating process [2,3].

As described in Section 4.1, one difference between the ITER boronization system in comparison with those in smaller devices is that some design aspects have been guided by physics simulations of the glow

discharge. Although the B coating replaces the O gettering role of Be, it is relatively short-lived. Too frequent deployment would eventually lead to a problem of fuel retention/dust (as was the case for the solid Be wall, which constituted an effectively infinite Be source) and it is actually on this basis that maximum allowable boronization frequency is established in the revised IRP. Section 4.2 addresses the issues of B layer lifetime (thus erosion/migration), with Sections 4.3 and 4.4 respectively discussing the associated fuel retention due to co-deposition and the possible fuel recovery mechanisms.

4.1. Boronization physics basis

Even though the first boronization process in a magnetic confinement device, using more-or-less the same approach adopted widely today, was developed on TEXTOR in 1989 [46], systems are usually based on empirical considerations and community experience. A plasma-assisted chemical vapour deposition process in which a thin a-B/C:H film is put down on plasma-facing surfaces, boronization is typically performed by fuelling a normal He glow discharge conditioning (GDC) plasma with diborane (B_2H_6 or B_2D_6) at a concentration in the range 10–15 % [47,48,49,50,51]. Numbers and locations of GDC anodes and diborane gas injection locations are often of order 2–4, with turbo pumping usually appropriately placed relative to gas feed points. Since standard GDC requires zero or very low residual magnetic fields, boronization will only be possible on ITER in short or long term maintenance periods (STM, LTM) when the current in the toroidal field coils can be ramped down to zero (but with the coils mostly still cooled to superconducting temperature). This fixes the maximum possible boronization frequency (once per 2 weeks) since ITER operation will be based on a cycle of 2-week blocks with 12 days of 2 shifts dedicated to experiments followed by a 2-day STM period.

Tokamak GDC plasmas behave as hollow cathode discharges with the cathode corresponding to the grounded wall surfaces and with the discharge sustained by fast electrons emitted by ion secondary electron emission at the walls. Commonly used wall ion currents in present devices are in the range 20 μA cm^{-2} (see [52] and references therein) which for ITER, including parts of the divertor (e.g. baffle and dome umbrella regions) and main chamber wall surfaces, requires total currents of ~200 A to be distributed between groups of anodes located in the port plug front end units (the Diagnostic First Wall (DFW)) at outboard upper and equatorial levels – see Fig. 4. Although the DFW is recessed (by 10 cm) with respect to the innermost FW panel radial position (and therefore sees no direct charged particle fluxes during tokamak plasma discharges), these anodes will nevertheless be rather close to the plasma at all times and are tightly enclosed in the surrounding DFW steel surfaces. There is much competition for space in these port plugs and so anode numbers must be kept to a minimum – currently 8 foreseen for SRO (fixed by the port plug configuration to be installed for this phase), increased to 11 for the DT phases. A consequence of the limited number is that each anode will source a large current (up to ~30 A), at least a factor 10 higher than commonly used in today's tokamaks. To this should be added the rather innovative anode design (Fig. 4), which is in the prototype stage, but which has never been tested on a working tokamak. Such tests are planned in advance of the SRO phase.

Given the restricted anode numbers, an important question is to which extent a uniform B coating will be possible in a device at the ITER scale. In addition, to assist the boronization system design (which has just passed the conceptual phase at the time of writing), physics guidance has been required concerning the optimum glow pressure and number and location of gas injection points. A first-of-kind modelling capability has been developed at IO to provide such an assessment. The details may be found in [52]. It is based on Monte Carlo tracing of diborane molecules in the GDC plasma, from the point of ionization or dissociation, taking into account elastic collisions with neutrals. The reaction products – B-carrying radicals and ions – are then assumed to subsequently coat the plasma-facing surfaces in the regions near their birth. The background plasma itself is generated with the 2D fluid model first applied to simulate ITER GDC plasmas in [53], but with modifications allowing the impact of the H (or D) from the diborane molecules on the He glow plasma parameters to be taken into account. As shown in [52], this can be a very important refinement. For example, for an H_2 content of 12 % in a majority He glow (corresponding to ~5 % diborane in the injected He/B_2H_6 gas mixture), the bulk plasma T_e reduces by a factor 2 in comparison with a pure He glow. This has a noticeable impact on the B deposition uniformity. Regarding the latter, the simulations show that He is preferred over a hydrogenic carrier; at fixed glow pressure, majority He glow plasmas have much higher bulk plasma T_e, leading to higher probability of diborane decomposition away from the anodes. Glow pressures around 0.3 Pa (found appropriate for reasonable glow plasma uniformity in [53]) are also important to maintain high bulk plasma T_e.

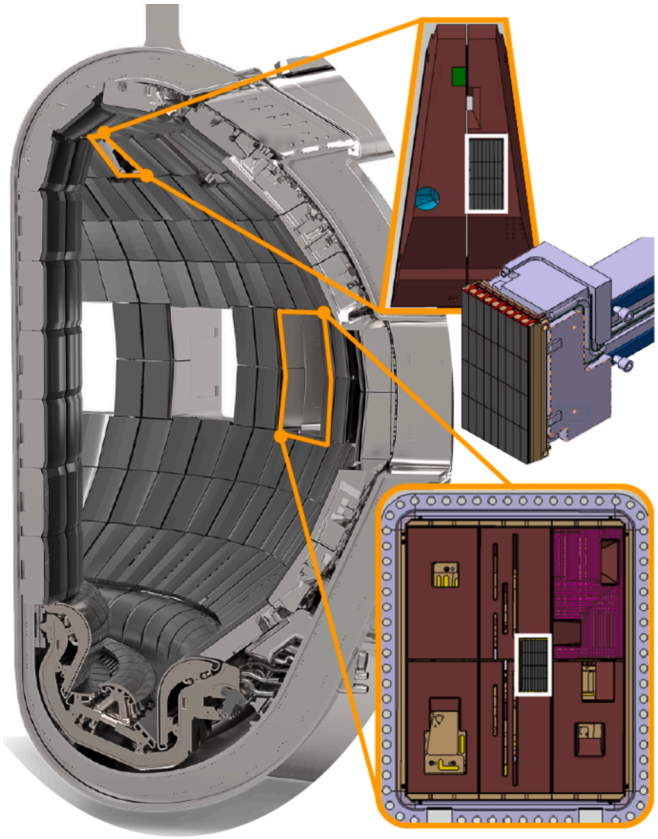

Fig. 4. Illustrating how the ITER GDC anodes will be embedded directly in the DFW at midplane and upper port locations. A CAD image of the current anode design is included for reference.

Fig. 5 provides an example of the boronization simulation model in action, addressing the particular case of the 2D toroidal-radial distributions of normalized diborane decomposition counts in the equatorial midplane for an 88 % He, 12 % H_2 mixture at 0.3 Pa neutral pressure for the two glow anode configurations currently expected for the SRO and DT-1 phases in the re-baseline. The 2D fluid model which is used to generate the glow plasma backgrounds cannot represent the real GDC geometry and instead approximates the vacuum vessel by a volume contained between two concentric spherical walls and works in cylindrical coordinates [53]. It is thus at present only possible to simulate a given radial-toroidal plane, chosen in the case of Fig. 5 to be at the centre of the glow anodes located in the outer midplane port plugs.

Although anode placements are enforced by the requirement to be housed in port plugs, the gas injection locations can be chosen more freely and are an input to the boronization system design. In the

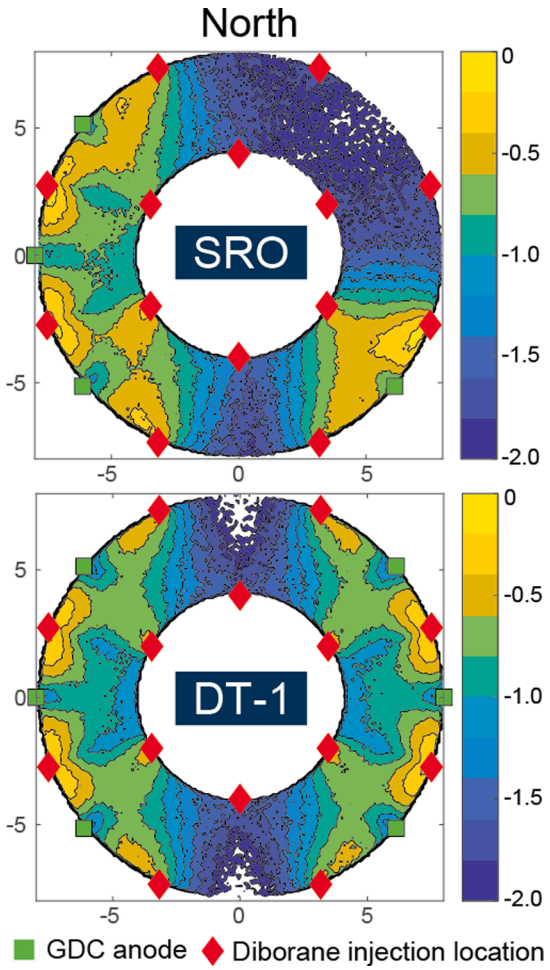

Fig. 5. Contour plots of normalized diborane reaction counts (log scale) in the equatorial midplane for an 88 % He / 12 % H_2 carrier gas mixture at 0.3 Pa glow pressure for the anticipated (a) SRO and (b) DT-1 GDC anode configurations (number and location of diborane gas injection locations are fixed for both cases). The reaction counts are normalized such that the surface integral is unity. Figure
adapted from [52].

examples of Fig. 5, the diborane is injected from both the low and high field sides at specific point-like toroidal locations (in practice in ITER, the gas will be injected through pipes recessed in the gaps between blanket modules and will not behave as point sources). This turns out to be very important in order to ensure reasonable coating thickness on the HFS. A separation of several metres between anodes and diborane injection points is also recommended by the simulations to improve coating uniformity, as is the injection of gas in places where anodes cannot be located. Such findings are essentially a consequence of the length scales for diborane decomposition, determined by the mean-free-path for disassociation and ionization (of order 3–4 m in these majority He glow plasmas) shortened to 1–2 m by elastic collisions of the diborane molecules with He neutrals [52].

Fig. 5 clearly demonstrates that the B layer in the midplane vicinity may be rather toroidally non-uniform for the SRO phase when the planned port plug configuration will mean that only one of the 3 anodes planned on the east side of torus at the equatorial midplane can be installed. This is compounded by the impossibility of locating anodes in the areas occupied by ports dedicated to NBI and EC/IC heating systems, leaving comparatively wide regions to the north and south sides with lower decomposition counts. A key question is therefore to which extent this matters: since the primary function seen for boronization on ITER is O gettering, rather than coating surfaces to reduce the W wall source, a significantly reduced B layer thickness in some areas may not be a major issue. Experiments on current full-W devices in which such coating uniformities are reproduced (e.g. by energizing only certain anodes) and the impact on subsequent operation is monitored, would thus be of great value and are being executed at the time of writing. Similarly, quantitative studies of B layer uniformity in current toroidal devices or well-defined laboratory experiments, along with some measurements of the glow plasma parameters, are required to validate the boronization modelling performed for ITER.

4.2. *Boron layer lifetime*

Closely related to the issue of B coating uniformity and its influence on reducing low-medium Z impurities is the question of layer lifetime following a boronization procedure. With regard to O gettering, based on [54], a 50 nm coating can bind ~1–5 x 10^{20} O atoms m^{-2}. For the expected ITER maximum impurity outgassing rates and a conservatively low estimate of the total in-vessel surface area (~10 % = 65 m^2) acting as an effective O gettering surface, a single boronization could correspond to a possible O storage capacity of 2.5 – 12.5 weeks of ITER operation [52]. The question is then how this compares with the expected erosion lifetime of the B coating.

Boron layer lifetime estimates have been made using the same WallDYN approach as described in Section 3 for the wall W source evaluation, but now performed with WallDYN3D [55], taking into account the 3D geometry of the ITER FW [30]. As mentioned earlier, unlike in the case of a pure W wall, where erosion is primarily on plasma wetted areas and is dominated by ion sputtering (Ne and W for the case of Ne seeded plasmas), for a B coating, erosion by fuel CXN in magnetically shadowed regions (which constitute the vast majority of the main chamber surfaces) is a significant contributor. In fact, once the B in wetted areas has been eroded, it is essentially the only contributor.

Fig. 6, extracted from [30], provides a visual representation of the qualitative time evolution of the erosion and migration of an initial 100 nm uniform B coating on a pure W bulk main chamber wall (coating assumed to be completely absent on divertor surfaces at t = 0) under plasma exposure to the same “worst case boundary plasma parameters” used in the WallDYN2D assessment for the burning plasma W wall source (Fig. 2). The simulation is only qualitative in the sense that the simplicity of the WallDYN surface model cannot quantitatively model the depletion of thick (~100 nm) B layers on the main chamber wall and at the same time correctly describe the re-distribution of the eroded B on divertor surfaces where it must ultimately all accumulate [30]. It does, however, demonstrate clearly how the main chamber initially remains coated up to the first ~1000 s of plasma exposure, with the eroded B depositing at the inner divertor target and the outer target baffle area. Thereafter, the main chamber coating begins to deplete (the B on plasma wetted areas is thus very quickly removed), the divertor deposition is re-eroded and the entire B source finally collects below the inner target where it can no longer be accessed by plasma fluxes. The entire evolution requires ~5 x 10^5 s.

Defining “lifetime” as corresponding to 10 % of the main chamber surface coating remaining, these dynamic WallDYN3D simulations yield that a single boronization depositing a uniform 100 nm layer on the ITER main chamber would last for ~10^5 s under exposure to worst case burning plasma conditions [30]. Since the ITER GDC boronization system design currently assumes ~50 nm coatings deposited in a single process (requiring ~11 h of glow plasma), this lifetime may be reduced to ~5 x 10^4 s. For the average rate of 13 successful pulses per day and 12 operational days per two week block assumed in the re-baselined IRP (see above and [10,11]), this corresponds to an average high power duration of ~320 s per pulse. This performance is not expected until the FPO-4,5 campaigns in the DT-1 phase (Fig. 1), but assuming the achievement of such operational conditions (which requires routine burning plasma operation, unhindered by issues of plasma start-up on W surfaces – see Section 5), then the B lifetime analysis, together with the

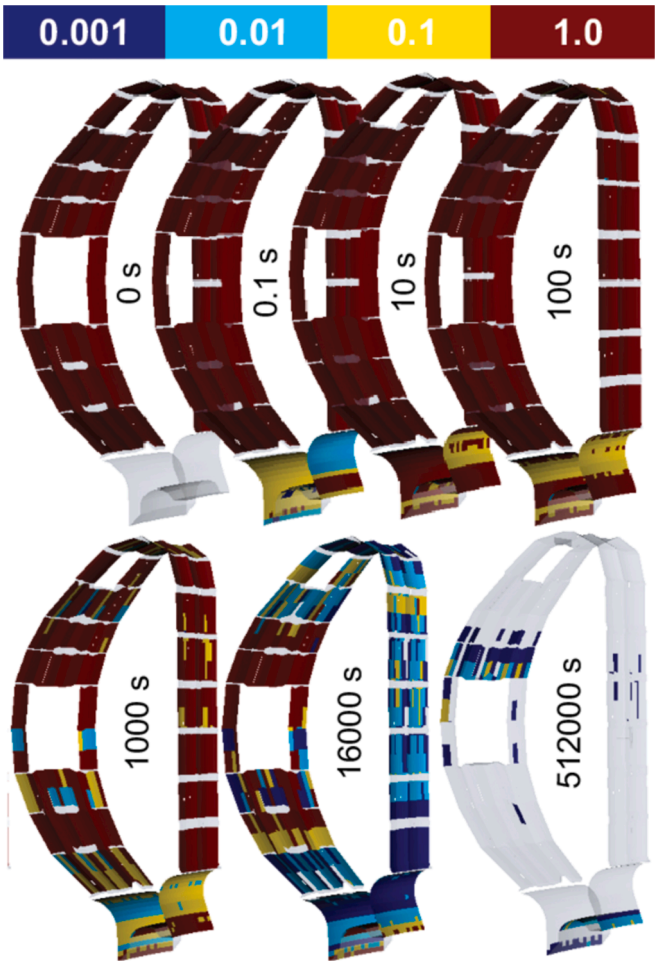

Fig. 6. Time evolution of B coating erosion and redeposition from a WallDYN3D simulation assuming the same worst case far-SOL plasma background used in the evaluation of the W wall source with WallDYN2D (see Fig. 2) and for an initial 100 nm thick, uniform B coating on a W main chamber wall (corresponding to a value of 1.0 in the colorbar). Figure reproduced from [30] with slight modification to graphical format.

worst case assumption for O uptake capacity, imply a maximum required boronization frequency (approximately every 2 weeks) which is entirely consistent with the planned ITER operation cycle.

This WallDYN lifetime analysis highlights another important difference when switching from Be to W in the re-baseline. Whereas with Be, the main chamber constitutes an effectively infinite erosion source, the maximum total quantity of B which can eventually migrate to remote areas (in the case of Fig. 6 to a location under the inner divertor) for a boronized full-W ITER is fixed by the quantity of injected boron. For a uniform 50 nm thick coating, this amounts to ~86 g per boronization. Adopting the maximum frequency of one boronization per two weeks and depending on precisely how the re-baselined IRP will actually be implemented, the maximum total dust quantity which could be generated in the DT-1 phase (FPO-1 to FPO-5 (Fig. 1)) is 13–15 kg, assuming (conservatively) 100 % of all B injected into the torus is eventually converted into dust. Whilst not negligible, this is at least an order of magnitude lower than previous estimates made on the basis of Be erosion and subsequent migration/re-deposition for the 2016 Baseline [56] and is far below the authorized regulatory limits for mobilizable dust [57]. An important related issue, discussed in Section 4.3, is how much T may eventually end up trapped in co-deposited layers and in this poorly accessible dust reservoir. This is in turn determined by the fuel recovery strategies which need to be deployed during the experimental campaigns themselves.

Finally, one further aspect of boronization not discussed here is the issue of potential coating of diagnostic first mirrors – the first elements of all ITER optical diagnostics located just behind apertures in the DFW. Although these systems are almost all equipped with shutters and mirror cleaning systems [58], so that the mirrors will be hidden during the boronization process itself, the B coating will be deposited over all DFW surfaces. Subsequent CXN sputtering of the coating in these recessed areas may push some B to migrate onto the mirror surfaces. If this occurs, it is thereafter a question of the balance between subsequent erosion and deposition on the mirror surfaces as to whether or not layers may grow and at what rate. This process has been analysed with the Monte Carlo impurity transport code ERO2 for the case of the W-Be material mix on ITER and realistic DFW geometries and found not to be an issue, for a plasma exposure period equivalent to the first 3 FPO campaigns of the 2016 Baseline [36]. A similar exercise is now required for B-coated DFW surfaces for the exposures planned in the re-baselined IRP. Of course, the same caveats regarding the uncertainty in the far SOL plasma background which apply to the W source and B lifetime calculations also apply to estimates of first mirror deposition.

4.3. Fuel retention

With Be eliminated, the main sources of T retention in a full-W ITER will be co-deposition with eroded and re-deposited B and W and implantation in W. Regarding B co-deposits, the migration simulations described in Section 4.2 provide the co-deposition source, but an estimate is required for the fuel uptake efficiency – the ratio of T/B in the co-deposits. Given the long intended use of Be on ITER, quite some effort has been dedicated to the fuel uptake of Be co-deposits, including the development of scalings for T/Be (using D as a proxy for the T) as a function of the main parameters observed empirically to determine the ratio. Namely substrate temperature, Be deposition rate and the fuel ion energy [59] and, more recently, including also the fuel background neutral pressure [60]. In contrast, despite its frequent use in today's devices in the form of boronization coatings, there is relatively sparse data for {H,D,T}/B.

A literature review conducted as part of the re-baseline activities is summarized in Fig. 7, which compiles data for the dependence on substrate temperature of the H content in B co-deposits found in laboratory experiments performed by the fusion and semiconductor communities.

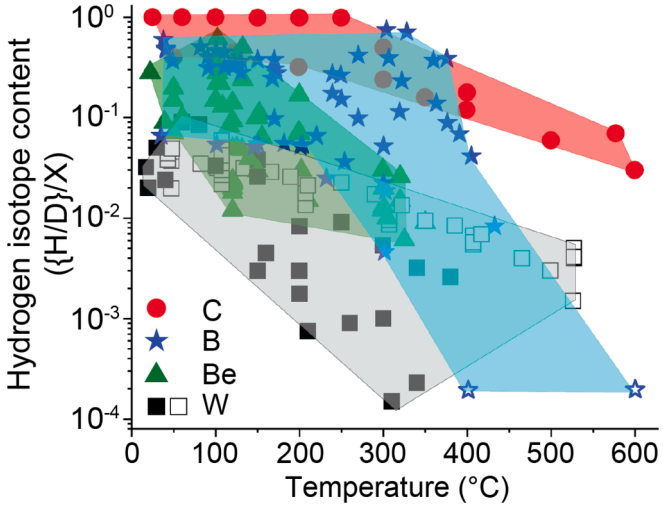

Fig. 7. Literature review of hydrogenic fuel retention by co-deposition as a function of co-deposit temperature for B layers and comparison with W, Be and C co-deposits. Data are extracted from the following published sources: H-B: [61 62 63 64 65]; D-W: [66 67 68 69] (NB: open squares: in-vacuo measured content, filled squares: post-mortem analyzed content); D-Be: [66 70 59 71]; D-C: [66].

There is little or no such laboratory data for D-B layers. Some points for W, Be and C co-deposits are also included for comparison. References to all data sources may be found in the figure caption. The B co-deposition in these studies is achieved via thermal or plasma decomposition of volatile B-C–H compounds (B_2H_6, $B_{10}H_{14}$, $B_2C_{10}H_{12}$) and most were concerned more by the mechanical, optical and electrical properties of films and not the H content.

In general, the H content in B layers is higher than that in Be and lower than in C. Boron layers from the very few available studies in tokamaks (not included in Fig. 7) indicate overall lower hydrogen content: ~0.1H/B in Alcator C-Mod in B layers at the inboard and outer divertors in a campaign with GDC boronization [72], whilst ASDEX Upgrade reports a content below 0.1H/B in B layers at the outer divertor and up to 0.2H/B at midplane limiters in B powder dropper experiments [73].

To ensure conservatism in T retention estimates for ITER, the tokamak data are ignored and a fixed value of {H/D/T}/B = 0.5 is assumed, consistent with Fig. 7. Boron co-deposits can thus retain a maximum of 4, 8 and 12 g of H, D and T per 50 nm boronization on ITER depositing 86 g of B (see Section 4.2). The maximum quantity of T retained per boronization is therefore 12 g × [%T/(%H+%D+%T)] where %X refers to the percentage of the respective isotope in the fuel mix. Applying these zero order scalings leads to an estimated total T retention in B co-deposits of 320 – 380 g by the end of the DT-1 phase, with the variance due to the different choices which might be made in the execution of the FPO-4 and 5 campaigns.

Fuel trapping by co-deposition with W will be dominated by the net erosion and local redeposition at the wall since, under burning plasma conditions (when T will be used), the divertor must be operated in partial detachment for target power fluxes to be manageable [13]. In this case, the low target plate electron temperatures and high densities will mean that W sputtering will be low and prompt redeposition high. Similarly, for divertor target integrity, ELMs must be strongly mitigated or suppressed during burning plasmas and so their contribution to a divertor W source should be low. To compute the total T retention in W co-deposits, fuelling rates and throughput are first estimated in a very simplified manner by scaling the various discharges and discharge numbers in the revised IRP [10] with I_p and $< n_e > / n_{GW}$ (n_{GW} is the Greenwald density) from reference values for the Q = 10 baseline, for which the peak stationary fuel throughput is 200 Pam^3s^{-1}. The worst case WallDYN2D integral gross erosion wall source from Section 2 (Fig. 2b) is ~1.4 x 10^{21} W atoms s^{-1} (~0.42 gs^{-1} W) which, according to the simulations, yields a net source an order of magnitude lower (~0.04 gs^{-1}). Taking a retention ratio of T/W ~0.05 (Fig. 7), gives a total T retention in W co-deposits of ~6.5 g at the end of the DT-1 phase (an additional small factor might also be added to account for a possible divertor W erosion source). Whilst there are obviously uncertainties in this estimate, it is at worst around a factor ~60 lower than the maximum retention due B co-deposition.

The final main fuel retention mechanism is through implantation and diffusion/trapping into the bulk plasma-facing material, for which the net retention scales with the square root of the particle fluence. Based on 2D simulations [74], for an integrated exposure to typical Q = 10 plasma conditions of 10^7 s, a total of 14 g H (i.e. 28 g D and 42 g pure T) would be retained in the W divertor. To convert this into the net retention expected through implantation during the different phases of the new IRP with a main chamber W wall, the divertor ion flux is scaled as for the co-deposition estimates (by I_p and n_e/n_{GW}) and the particle flux to the wall is conservatively taken as 20 % of the total to the divertor. This gives a total T retention by implantation of between ~18 – 24 g by the end of the DT-1 phase.

4.4. Fuel recovery

The issue of fuel removal is evidently a key aspect of ITER exploitation and developing a quantitative strategy for removal is a long term, ongoing activity at IO. Although the situation changes somewhat with the elimination of Be in the re-baseline, the key fuel recovery techniques that can be applied during and in-between campaigns remain unchanged: isotope exchange and heating of deposits/surfaces. For the former, the main tool currently envisaged is by plasma operation and ICWC (and combinations of both), whilst for the latter, static baking and the use of special plasma configurations to raise surface (and co-deposit) temperatures are the principal options.

The updated IRP includes an allocation of 15 % of operational time dedicated to T removal within each series of DT experiments [10,11]. Importantly, since the STM periods at the end of each 2-week experimental block within a given campaign in the DT phases are far too short for baking to be an option, it is only the “active” techniques, i.e. ICWC, GDC and specific plasma operation scenarios (for example the Raised Inner Strike Point (RISP) configurations pioneered at JET to heat up inner divertor baffle Be co-deposits [75,76] and considered an option for ITER [77]) which can be deployed. Furthermore, since fuel implanted in surfaces and diffusing beyond the reach (≳ 1 μm) of isotope exchange by plasma exposure or ICWC, can really only be accessed (at least partly) by baking, and because retention will be dominated by co-deposition with B if ITER is routinely boronized (Section 4.3), it is really the inventory in co-deposits which is the main objective of these active recovery methods.

On the basis of physics analysis and empirical observations, the detailed discussion of which is beyond the scope of the present paper, a removal efficiency of 70–80% from deposits and implanted T is set as a target within the DT-1 FPO campaigns. The specific case of recovery by baking, which can only be performed prior to LTM periods, will be considered in more detail below given that it was also the focus of R&D in the previous baseline when considering slow outgassing of thick Be co-deposits. It will be found that the same issues faced by Be of only partial recovery will be encountered if B deposits are allowed to accumulate without routine application of active techniques within experimental blocks.

At a 70–80 % active recovery efficiency (thus excluding baking at the ends of operational campaigns), taking into account the estimates in Section 4.3 for the magnitude of retention through co-deposition and implantation (therefore assuming the maximum number of boronizations), the total expected in-vessel T-inventory is conservatively expected to be in the range ~95 – 114 g at the end of the DT-1 phase. The corresponding range of total injected T is ~226 – 335 kg, giving target long term retention rates of just ~0.03 – 0.04%.

At present, JET (with Be/W PFCs) is the only device on which extensive, ITER-relevant fuel removal strategies have been tested, benefiting in particular from the recent DT campaigns [75,76]. The well-known early results from the first ITER-Like Wall experiments found that 2% of injected fuel is retained based on gas balance analysis [78], while post-mortem analysis finds 0.2% retention [79]. In the recent JET DTE2 experiments, a total quantity of 252 g-T was injected which, if the findings in [78,79] apply, implies 0.5 – 5 g of T being permanently retained. The detailed T-removal sequence which followed the campaign, consisting of baking, ICWC, GDC and tokamak plasma, removed about 0.7 g [76], which translates to a fuel removal efficiency of 14–140%. That the target estimated long term retention rates for ITER’s DT-1 phase are somewhat lower (~factor 5) than the measured values from JET can be attributed to the fact that in ITER, the dominant mechanism of fuel co-deposition with B is fixed by the number of boronizations, whilst in JET (and in the previous ITER baseline), there is a continuous main chamber erosion source of Be. Furthermore, since W erosion in a full W ITER is expected to be low and T co-deposition in W is much lower than in B, the overall long term retention should be considerably reduced.

Returning to the issue of thermal outgassing of co-deposits, it has only been realised comparatively recently that the efficiency of baking for T removal from Be co-deposits could be considerably more difficult than initially thought if thick co-deposit layers would accumulate in

certain areas (as is predicted for ITER and found experimentally to occur readily on JET with Be main walls [80]). The thermal efficiency for T-removal from Be co-deposits was analysed using the TMAP7 code, setting model parameters by reproducing thermal desorption spectra obtained from JET co-deposits [81]. It was concluded that the efficiency of the planned 350°C divertor bake in ITER would be limited for thick (> 50 μm) co-deposits, and that significant baking durations (~1 month) would be required to remove meaningful fractions of retained T. This 350°C ITER divertor baking temperature (to be achieved using high temperature nitrogen gas circulating in the divertor cooling circuits) was originally chosen on the basis of laboratory Be-D co-deposition studies for rather thin layers (see e.g. [70]).

To examine the impact of layer thickness on thermal outgassing in the case of B co-deposits, the same approach as in [81] has been adopted but now using the CRDS [82] and MHIMS [83] trapping-diffusion codes. The configurations and parameters of the standard trapping-diffusion models within these codes that can reproduce selected literature data on thermal desorption of B:D layers are first established and the codes then applied to evaluate the fuel removal efficiency from layers with different thicknesses and at different temperatures. As discussed in Section 4.3 (Fig. 7), whilst comparatively good datasets are available for thermal outgassing of Be co-deposits, the literature is rather sparse for the case of B layers. Experimental thermal desorption spectra for D outgassing from B layers in [84,85,86] are used for the simulations (note that the data from these studies could not be included in Fig. 7, since they are only in the form of thermal desorption curves and not {H,D}/B ratios).

To reproduce the experimental data, the trapping parameters (trap energy and relative trap density) are obtained assuming fast diffusion, release dominated by de-trapping and re-trapping, instantaneous surface desorption and a no flux condition at the substrate side. While CRDS assumes saturated traps to reproduce the desorption curves in [84], an initial depth profile from SIMS is used to match the data in [85]. In the case of the data reported in [86], MHIMS simulates the implantation phase of D ions.

With CRDS using a 2-trap model, de-trapping energies of 1.1 eV and 1.5 eV are required to match the data in [84], whilst energies up to 2.15 eV are required to reproduce the curves in [85]. Using MHIMS, de-trapping energies between 1.05 eV and 1.59 eV for a 4-trap model are obtained for the data in [86]. The derived trap concentrations lead to D/B ratios in the 0.5 – 1.6 range.

To investigate the efficiency of thermal fuel removal, the two codes have been run using the trap energies and densities obtained from this fitting of the TDS spectra and assuming an initial uniform depth profile with D/B = 0.5 to compute the release fractions for a 2 week bake at temperatures between 210—350°C with B layer thicknesses from 0.1 – 50 μm. Results are compiled in Fig. 8.

Evidently, the released fractions increase with increasing bake temperature and decrease strongly with layer thickness. It is also clear that the removal fraction varies significantly depending on the laboratory data used to derive the trap parameters. In general, it may nevertheless be concluded that divertor baking within the range of temperatures that could potentially be achieved on ITER (240°C by water baking 350°C by gas baking) will have limited efficiency for the removal of the thick B layers expected to form during ITER experimental campaigns if boronization is used frequently. In particular, it is difficult to remove fuel from a trap with the de-trapping energy of 2.15 eV required to fit the data from [85]. On the basis of this preliminary analysis, the efficiency for thermal desorption appears limited for anything but very thin layers (hundreds of nm). Moreover, long bake durations (> 1 month) might be required to remove significant fractions of retained T from thicker layers. This is a very similar conclusion to that reached for Be co-deposits [81]. In view of these findings and the significant technical complexities associated with the 350°C divertor hot gas bake, it is proposed to remove this capability in the re-baseline. In this case, the water cooling circuits will be used to provide a maximum main chamber and

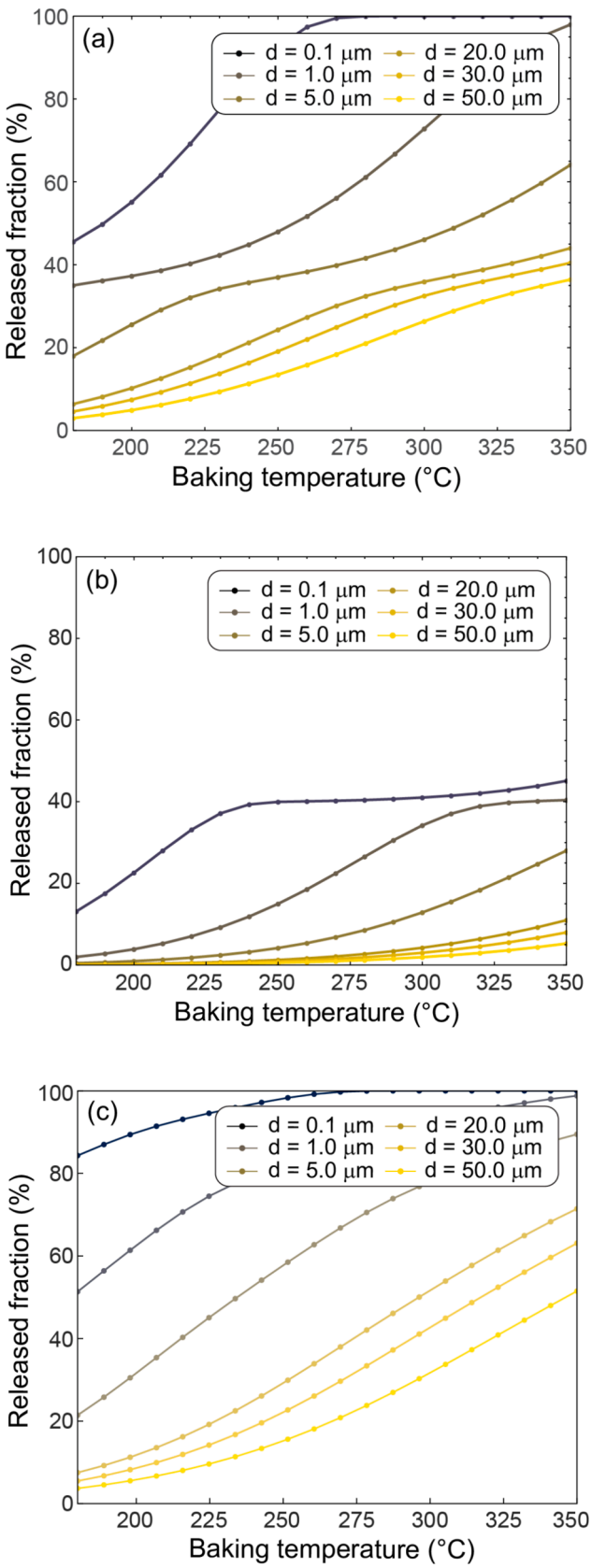

Fig. 8. Simulations of thermal release from B co-deposit layers during 2 weeks of baking as a function of layer thickness and baking temperature using two different diffusion-trapping codes: CRDS code using model set-up and parameters based on (a) data in [84] and (b) data in [85]; (c) MHIMS code based on data extracted from [86].

divertor baking temperature of 240°C.

According to the B migration simulations described in Section 4.2, deposits are expected to accumulate in the divertor (as also observed in current devices, e.g. [79]). They will also be the main reservoir for fuel retention in the full-W ITER. The thickness of these deposits will depend on their poloidal extent, itself dependent on the details of the far SOL plasma background, but could reach several microns after each boronization cycle. Since baking can be used only in LTM periods, very thick co-deposits may easily grow through a given experimental campaign. It will thus be important to perform routine fuel recovery strategies throughout the operational cycle to avoid the accumulation of T in these layers. This will also ensure that if the eroded B coating does finally migrate to the bottom of the machine (Fig. 7) in regions inaccessible to plasma conditioning, it does so without any significant T inventory.

The RISP approach mentioned above is one promising option for detritiation of B co-deposits accumulating in the inner divertor baffle regions, particularly given that the contact resistance of these layers with the substrate may be rather high, as found for Be co-deposits on the JET inner divertor [75]. This should allow relatively low power RISP plasmas to raise the layer temperature to rather high values (for example, a maximum temperature of 1280°C for a duration ~10 s was achieved for Be deposits on the W-coated CFC tiles in the JET inner divertor baffle region using this method [76]). Application of the CRDS and MHIMS trapping-diffusion codes in the same way as performed for the baking efficiency analysis in Fig. 8 finds that, depending on the model parameters, 10 s of plasma exposure at 1000°C is sufficient to fully deplete a 5 μm thick B layer. The higher the temperature, the more effective the fuel removal process becomes. These same simulations also indicate that extending the time of heating at high temperature brings minimal gain in removal efficiency.

Since some fuel co-deposition with B would also occur during RISP plasmas themselves, potentially away from the divertor, the T content in the new deposits must also be removed. This could be achieved by depleting the accessible T prior to and after a RISP pulse using, for example, isotope exchange with ICWC. For main chamber deposits, it may also be possible to deploy something similar to the "limiter cycling" pulses which have been routinely used at JET in recent years [76], though these can only really access deposits in plasma wetted areas.

To improve estimates of the fuel retention and release from B co-deposits, dedicated laboratory studies are required to generate a database for fuel uptake in the same way that has been performed for Be (see [59,60]). This will then allow scalings for the {D,T}/B ratio to be developed for use within the migration and diffusion trapping codes. In addition, better experimental characterization of real tokamak B co-deposits would be of great value to the quantitative development of the ITER fuel recovery strategy.

5. Limiter plasma start-up on tungsten

On ITER, as in many tokamaks, plasma start-up will be performed in limiter configuration on the inboard equatorial FW panels. Whereas for the Be FW, the concern was more for long wave misalignments leading to power loads locally exceeding power handling capabilities [1], in the case of W it is the potential for very strong radiative losses in these early phase plasmas which poses the highest risk to successful start-up.

In the very early phases of the current ramp-up, temperatures in the plasma edge can be easily sufficient for W to be released by physical sputtering due to fuel and impurity ion impact. As a consequence of the limiter configuration, the sputtered W neutrals may reach the confined plasma much more readily than in the diverted phases and can be ionized up to high charge states. On their return to the limiter surface, these W ions are accelerated to high energies ($E_i \propto 3Z_iT_e$) across the plasma sheath. Since W self-sputtering yields can easily exceed unity for such impact energies, the W core concentration can rise very rapidly in the initial phase of the limiter start-up. The situation is aggravated by the presence of light impurities due to their higher W sputtering yields in comparison with hydrogen isotopes. Oxygen is a particularly common example and is often present in small concentrations in the vacuum of most tokamaks, even following the usual wall conditioning steps (e.g. baking, glow discharge). Reducing such residual O levels is the principal driver behind the addition of a boronization system in the ITER re-baseline (Section 4).

As will be seen in the sections below, the plasma-W system is expected to a large extent to be self-regulating, since the initial high W release once closed flux surfaces are formed and wall contact occurs leads to strong radiative losses, which in turn reduces the edge temperature and hence the sputtered flux. In a stationary (time independent) system, the SOL plasma solution will tend to an equilibrium with an average W self-sputtering yield of unity. The issue, in the real situation, is whether or not the plasma will pass through this difficult early phase in terms of the overall power balance. Experience from current devices is rather limited in the sense that only very few tokamaks have performed plasma current ramp-up on W surfaces. It was already routinely demonstrated on ASDEX Upgrade in 2008, even immediately after long term vacuum vessel venting and without boronization [87,88]. This is obtained by careful tailoring of the density and early EC heating, with the earliest possible divertor transition (note that on ITER, limiter plasmas of up to ~10 s are expected to be required before X-point formation [1], cf. ~0.4 s on ASDEX Upgrade). From 2013 onwards, the progressive installation [88] of steel (Eurofer) tiles on the inner midplane [89] means that ASDEX Upgrade no longer starts plasma on HFS W surfaces, though a return to W inner wall tiles is currently planned for 2025.

On WEST, when operations with the full-W wall began, start-up was found to be rather problematic on the W inner bumper limiters, with early nitrogen (N) injection used as a mitigation strategy [90]. The tiles were ultimately exchanged for boron nitride (BN) units at the end of WEST Phase 1 (Campaign C5), but have since been observed to coat with W eroded from elsewhere in the device. Meanwhile, start-up recipes have been improved so that limiter ramp-up on these quasi-W surfaces is now possible without resorting, for example, to N seeding. At the time of writing, WEST has completed the installation of new bulk W tiles in the start-up areas and is presently conducting limiter ramp-up experiments following the maintenance shutdown during which the tiles were introduced. Section 5.3 will describe some of the key findings from new W limiter start-up experiments on the EAST tokamak, performed specifically in support of the ITER re-baseline.

The limiter phase in modern research tokamaks is usually rather short (hundreds of ms), dynamic and of little interest, particularly in the case of low Z PFCs. It is almost never modelled. With W, and given the comparatively long limiter phase on ITER, simulations are required which not only account properly for the plasma boundary interactions (including W impurities), but which are also capable of modelling the scenario development through the ramp-up in terms of magnetic control. In addition, neoclassical transport is extremely important for high Z impurities and realistic simulations must at least include a reasonable core transport description. Ideally, all three components would be combined in a single integrated model capable of time-dependent simulations from edge to core throughout the limiter phase. This is not yet possible with high fidelity, so a combined approach using the SOLPS-ITER, DINA and JINTRAC codes has been used to make some first assessments for ITER. These modelling efforts are described below in Sections 5.1 and 5.2.

5.1. SOLPS-ITER and DINA tungsten limiter plasma modelling

The 1.5D DINA code [91] has been the main workhorse for scenario simulations on ITER and is a particularly important tool for all aspects of magnetic control. It comprises a 2D free boundary plasma equilibrium solver and 1D model describing transport of the poloidal magnetic flux and the plasma temperatures (electrons and ions). The code simulations take into account eddy currents in the vacuum vessel, models of the

power supplies, engineering limits imposed on the central solenoid (CS) and poloidal field (PF) coils, plasma-wall gaps and divertor strike points, as well as feedback and feedforward control of plasma current, position and shape. As described in more detail below, it also contains a simplified description of the plasma-wall interaction in the limiter phases of current ramp-up, using zero dimensional power balance to determine heat fluxes and plasma temperatures, $T_{e,LCFS}$ at the last closed flux surface (LCFS). A sputtering model based on standard Behrisch/Eckstein yields [92] is included, with a correction of the normal incidence yields to account for surface roughness and sheath straightening of ion orbits. Both fuel and impurity ion sputtering is included. The radial density profiles of all impurities with given ionization state are calculated on each magnetic surface assuming coronal equilibrium and cross-field transport driven by diffusion and a pinch velocity.

To improve the fidelity of the simple 0D DINA boundary model for the limiter phase, a database of SOLPS-ITER (B2.5-Eirene) simulations has been generated from which scalings can be derived to refine the DINA boundary conditions, in particular $T_{e,LCFS}$. These same simulations also allow the prescription of a "screening factor" to be applied to the DINA 0D impurity influx to account for the (at least) 2D nature of the real situation. They are first-of-a-kind code runs in the sense that the ITER limiter phase has never previously been modelled with SOLPS-ITER, but also because they include W sputtering and transport.

The time-dependent evolution of the ramp-up phase cannot be captured in SOLPS-ITER so the focus is instead on stationary simulations performed on a single, moderately elongated magnetic equilibrium roughly halfway through the limiter phase of a full DINA end-to-end hydrogen L-mode scenario (see below and Fig. 11) to I_p = 15 MA (B_T = 5.3 T) – a discharge representing one of the principal milestones of the SRO phase (Section 2). Shown in Fig. 9a, the numerical grid is extended deep into the core plasma to provide meaningful data for the average W core concentration. At this point in the DINA scenario, I_p = 2 MA with a core heating power (ECH + ohmic) of ~3.3 MW. Cross-field anomalous core transport profiles are fixed in accordance with the scalings used in DINA, whilst in the SOL, they are designed to approximately match the expected double exponential parallel heat flux profiles for inner wall limiter plasmas based on the scalings derived for ITER [93]. The ECH power is distributed evenly from the inner boundary of the grid to a

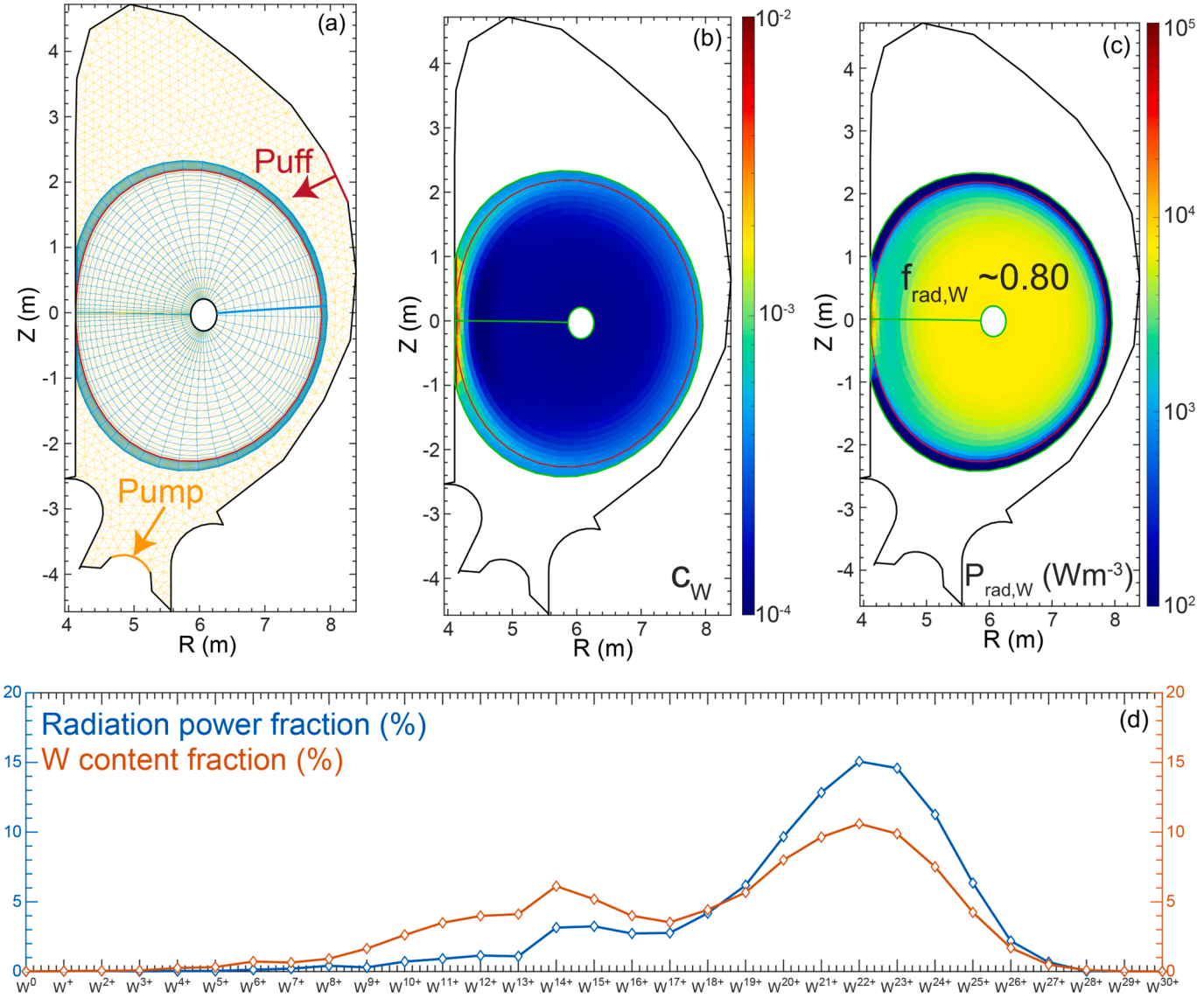

Fig. 9. Summary of output for a single SOLPS-ITER W limiter hydrogen plasma simulation from the main database with P_{in} = 3 MW, $<n_{e,LCFS}>$ = 2 x 10^{18} m^{-3}, I_p = 2 MA, B_T = 5.3 T: (a) numerical grid with gas puffing and pumping surfaces; poloidal distributions of (b) $c_W = n_w / n_e$ and (c) radiated power due to W; (d) charge state distribution and fraction of the associated radiated power up to the maximum charge state (W^{30+}) followed in the simulation. Magnetic equilibrium extracted at t = 4.9 s from DINA IMAS database shot 135011, run 7.

normalized radius of $\rho = 0.6$, though the final equilibrium solutions are not very sensitive to this distribution. More central heating (typically between $\rho = 0 - 0.2$) is generally applied in DINA simulations, assumed on the basis of experience on tokamaks working with W PFCs to be necessary to prevent core W accumulation (see e.g. [87] and Section 5.3 for new results from EAST demonstrating this directly in W limiter plasmas). This is also found to be required in JINTRAC integrated modelling (Section 5.2).

The SOLPS-ITER simulation database includes variations in heating power ($P_{in} = 2.2 - 5.5$ MW) and scans of the SOL cross-field transport coefficient magnitude (varying up and down by a factor of 2 from the "standard" profiles which are tuned to generate a $q_{||}$ profile consistent with the chosen $I_p = 2$ MA reference case). For each set of P_{in} and SOL transport choices, the plasma density is varied by changing the (hydrogen) gas puff rate, with each scan containing around 4–6 stationary solutions. Prompt redeposition of W is set to zero (the most conservative assumption) and is not expected to be very significant under these limiter SOL conditions, though this is an assumption which should be checked by dedicated simulations with appropriate impurity transport codes (e.g. ERO).

As shown in Fig. 9b,c for the example simulation at $P_{in} = 3$ MW and $<n_{e,LCFS}> = 2 \times 10^{18}$ m^{-3}, the W content is sustained in these runs by FW erosion, dominated by self-sputtering and leading to high radiative fractions, $f_{rad} = P_{rad}/P_{in} \sim 0.8$ and peak W concentrations, $c_W = n_W/n_e$ up to 10^{-2} in the plasma-limiter interaction area. Here, $<n_{e,LCFS}>$ denotes a poloidal average of the density around the first SOL ring of the numerical grid. Contributions to W release from H ions and CXN are found to be negligible in all simulated conditions. Based on some early test runs, the core temperatures achieved were such that the database simulations could be restricted to following W charge-states up to W^{30+} (no bundling assumed, unlike in the JINTRAC simulations described in Section 5.2). Fig. 9d shows the fractions of radiated power and W content for charge states up to W^{30+} demonstrating that this is a sufficient assumption.

The single simulation data point of Fig. 9 is identified in the database plots of Fig. 10a,b, which illustrate respectively the range of equilibrium P_{SOL} and f_{rad} obtained in the scans. Both depend weakly on the magnitude of P_{in} and its distribution. The most obvious dependence for P_{SOL} is found on the SOL transport coefficients, and even then the impression is only of a shift with respect to $<n_{e,LCFS}>$.

The robust behaviour of the radiated fraction ($f_{rad} \sim 0.7$–0.9) throughout the database is a manifestation of the strong self-regulation of the plasma-limiter system. The equilibrium P_{SOL} values correspond to a system with an average W self-sputtering yield of $< Y_{W\text{-}W}> = 1$, to which the system is naturally attracted if W is the only impurity. For a given input (including importantly the fuelling rate, which controls the plasma density), there is always one equilibrium SOL solution which constrains the resulting P_{SOL} and which in turn (along with the core transport profile and the W cooling function), determines the core W content required to dissipate the remaining power ($P_{in} - P_{SOL}$). The resulting average core W concentration, (not shown) is in the range $0.5 - 8 \times 10^{-4}$ and decreases with increasing density since P_{rad} ($= P_{in} - P_{SOL}$) $\sim n_e n_W$.

The average core W concentration, (not shown) is in the range $0.5 - 8 \times 10^{-4}$ and is self-regulated to provide $P_{rad} = P_{in} - P_{SOL}$. It therefore decreases with increasing density since $P_{rad} \sim n_e n_W$. The average W charge state at the LCFS, $<Z_{W,LCFS}> \sim 13 \rightarrow 9$ from the lowest to the highest $<n_{e,LCFS}>$ in the database (also not shown in Fig. 10), is found to be $\sim 1.5 - 2$ times higher than at the limiter itself ($<Z_{W,limiter}> \sim 8 \rightarrow 5$). This is not due to the recombination of W ions leaving the main plasma, but because, even at the lowest densities, more than 50% of the eroded W is ionized within the SOL, driving the average charge there downwards.

The key output from the SOLPS-ITER limiter database is the relationship between the poloidally averaged equilibrium $<T_{e,LCFS}>$ and $<n_{e,LCFS}>$ shown in Fig. 10c. Least squares regression finds the fit line:

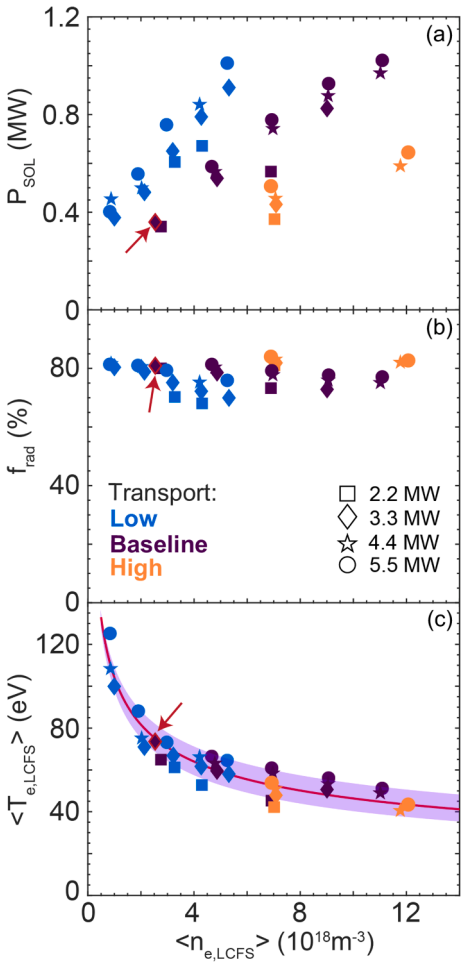

Fig. 10. Dependence on $<n_{e,LCFS}>$ of (a) P_{SOL}, (b) f_{rad} and (c) $<T_{e,LCFS}>$ for the SOLPS-ITER W limiter database. Each point represents a single converged SOLPS-ITER simulation. Colours and symbols represent respectively the magnitude of SOL radial transport and P_{in}. The small arrow in each plot identifies the single simulation case described in Fig. 9. In (c), the shaded region represents the 95% confidence interval of the fit line (Eq. (5.1)). All data are for H fuel with W as the only impurity, $I_p = 2$ MA, $B_T = 5.3$ T and the same numerical grid as in Fig. 9a.

$$\langle T_{e,LCFS} \rangle \, [\mathrm{eV}] = 104.2 \times \langle n_{e,LCFS} \rangle^{-0.35} \, [10^{18} \mathrm{m}^{-3}] \tag{5.1}$$

with the shaded region giving the 95% confidence interval on the fit. Note that there are no values of $<T_{e,LCFS}> < 40$ eV in the database, which is restricted to the lower fuelling (or density) region for which $<Z_{W,limiter}> > 5$ so that the W self-sputtering is dominated by sheath acceleration. At higher densities, both $<T_{e,LCFS}>$ and $<Z_{W,limiter}>$ are too low to achieve $<Y_{W\text{-}W}> = 1$, so that this regime is attained in the code as a result of the frictional coupling between the H and W flows to the target plate, driving supersonic W flow to the plate. The very existence of this high density behaviour is thus dependent on the SOLPS-ITER boundary condition for the impurity ion flow speed at the sheath entrance and is questionable. Moreover, this regime corresponds to $n_{GW} > 50$ %, even at the highest values of I_p (~ 3.5 MA) expected during the limiter ramp-up phase. This is unlikely to be routinely used during ITER start-up which should minimize the density in this phase to avoid too high radiation losses.

The $<T_{e,LCFS}>(<n_{e,LCFS}>)$ relationship in Eq. (5.1) has been used to refine the 0D DINA boundary model for the limiter phase which *prescribes* $n_{e,LCFS}$ and relates $T_{e,LCFS}$ to P_{SOL} through simple 0D power balance (note that DINA does not distinguish ion and electron temperatures at the LCFS, so by default $T_i = T_e$, but $T_{e,LCFS}$ will continue to be used

below for consistency with SOLPS-ITER and the averaging notation (< >) is henceforth dropped):

$$T_{e,LCFS}^{3/2} = P_{SOL} \Big/ \left(n_{e,LCFS} \gamma (k_B/(2m_i))^{1/2} 4\pi R_{OMP} \lambda_{q,eff} (B_p/B)_{OMP} \right) \quad (5.2)$$

where $\lambda_{q,eff}$ is an effective power decay length (which corresponds to the "conventional" λ_q in the case of single-exponential and, for a double-exponential SOL heat flux structure, to $(\lambda_{q,main} + R_q\lambda_{q,near})/(1 + R_q)$, with R_q a measure of the power carried in the narrow (near-SOL) power channel (of radial width $\lambda_{q,near}$) [93], R_{OMP} is the outer midplane major radius, B, B_p are respectively the total and poloidal magnetic fields at the same location, γ is the sheath transmission factor, $\lambda_{q,main}$ is the characteristic radial width of the main SOL parallel heat flux, k_B the Boltzmann constant and m_i the fuel ion mass. In the DINA model, the value of $T_{e,LCFS}$ obtained from Eq. (5.2) is used to estimate the average impact of energy of ions arriving at the limiter, $E_0 = (2 + 3 <Z_i>)T_{e,LCFS}$ which is then used to obtain the respective sputtering yields, e.g. $<Y_{H\text{-}W}>$, $<Y_{O\text{-}W}>$, $<Y_{W\text{-}W}>$ etc., for all species included in a given simulation. The neutral W influx and ion outfluxes to and from the core plasma are linked through $\Gamma_{W0} = \sum \Gamma_i <Y_{i\text{-}W}>$.

This simplified approach has two main drawbacks. First, it uses a $T_{e,LCFS}$ corresponding to the plasma temperature at the tangency point to estimate erosion, whilst in reality, in 2D the erosion area is shifted outwards to a location where $T_e < T_{e,LCFS}$. Second, it does not account for the SOL screening of the eroded material. To bring the DINA erosion model in line with the SOLPS-ITER results, a further correction coefficient α is therefore introduced in the calculation of the mean ion energy: $E_0 = \alpha\ (n_{e,LCFS}, T_{e,LCFS})(2 + 3 <Z_i>)T_{e,LCFS}$. Its role is to ensure $<Y_{W\text{-}W}> = 1$ at the equilibrium combinations of $(n_{e,LCFS}, T_{e,LCFS})$ found in the SOLPS-ITER stationary solutions (Eq. (5.1) and Fig. 10c). It bundles the effect of the plasma-wall interaction occurring mostly away from the tangency point and the SOL screening of the sputtered impurity into a single coefficient which can be used to renormalize the DINA $T_{e,LCFS}$. Coefficient α can be expressed as $\alpha = T_0/T_{e,LCFS}(n_{e,LCFS})$, where T_0 is the temperature corresponding to the equilibration of the W self-sputtering: $<Y_{W\text{-}W}>((2 + 3 <Z_w>(T_0))T_0) = 1$. With this modification the DINA boundary conditions drive the steady-solution to the same equilibrium SOL parameters as found in SOLPS-ITER via an increase/decrease in the W source and associated radiation losses as $T_{e,LCFS}$ deviates from the equilibrium value. This model can also be used in the presence of the other impurities (such as O) if the particle flux profile of these impurities at the limiter is similar to that of the W.

A sanity check for the updated boundary conditions has been performed by running a time-dependent DINA simulation (up to t = 20 s), keeping the plasma shape and magnetic configuration as close as possible to the one used as a reference case for building the SOLPS-ITER database until stationary conditions are reached at $I_p = 2$ MA ($P_{in} = 2.2$ MW). Parameter $\lambda_{q,eff}$ was also tuned to the SOLPS-ITER value. With the new boundary condition, the DINA $f_{rad} = 0.71$ is in reasonable agreement with the SOLPS-ITER value (0.77) for a $T_{e,LCFS} = 55$ eV (by definition the same value for both DINA and SOLPS-ITER). The differences in f_{rad} originate essentially from the density profile shape which is prescribed in DINA, but controlled by the ionization profile in SOLPS-ITER. This profile difference drives a discrepancy in $<c_W>$, since at the lower $<n_e>$ obtained with DINA, more W is required to provide enough dissipation for $T_{e,LCFS}$ to be brought to the equilibrium temperature enforced by the new boundary condition scaling.

Equipped with the modified boundary condition, DINA has been used to study in detail one of the principal deliverables of the SRO phase in the re-baseline (Fig. 1): a hydrogen L-mode to 15 MA at $B_T = 5.3$ T. Fig. 11a summarizes various key power waveforms for the full end-to-end time dependence of key discharge parameters for one example scenario, with the first 20 s expanded in Fig. 11b to focus on the limiter ramp-up phase and including additional information on impurity concentrations and the plasma density evolution. The scenario passes through the reference equilibrium used for the SOLPS-ITER modelling

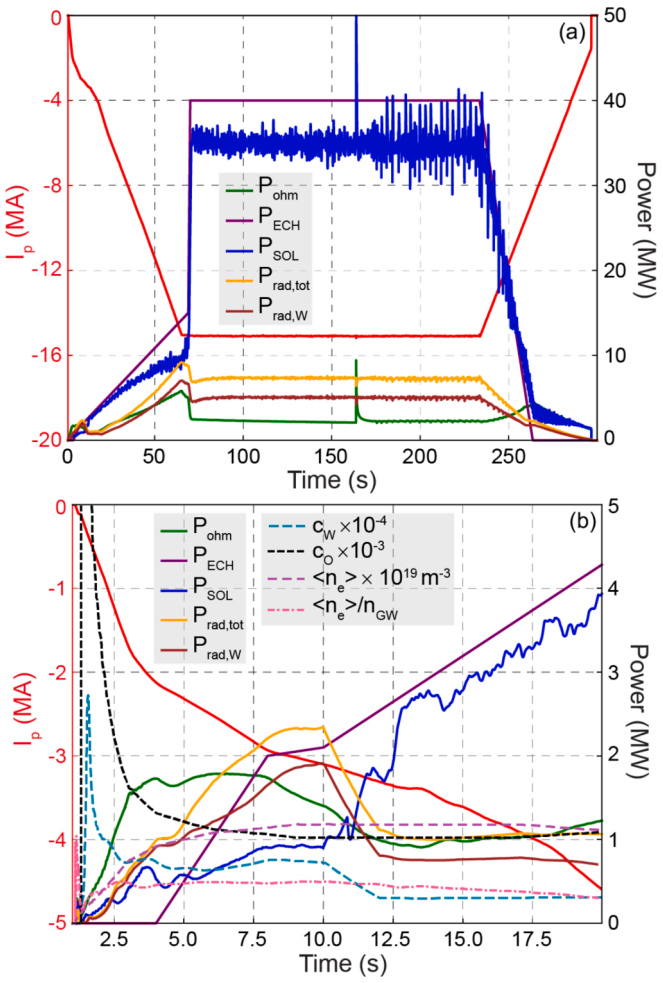

Fig. 11. End-to-end DINA scenario (DINA IMAS database shot 105069, run 2) for a hydrogen L-mode to 15 MA at 5.3 T computed using the new boundary condition on $T_{e,LFCS}$, derived from the SOLPS-ITER limiter simulation database (Fig. 10c, Eq. (5.1)) and with an assumed constant volume averaged O density, $<n_O> = 1.2 \times 10^{16}$ m^{-3} during the limiter phase: (a) main components of the power balance with the I_p waveform – the oscillations on P_{SOL} from t ~164 s are due to sawteeth. Note that the first large spike corresponds to the first sawtooth which, in the simulation, produces strong variation of the plasma current profile during a single time step of the simulation (10 ms) and in turn provokes a high, and unphysical spike in P_{ohm} ; (b) expanded region covering start-up, early current rise in limiter configuration with X-point transition at t = 10 s, including W and O impurity concentrations and plasma density waveforms.

described above (Fig. 9a) at t ~4 s and reaches full bore at t = 10 s at the transition to X-point configuration. More detail may be found in [94].

To account for possible O impurity during start-up (readily providing an initial source of W impurity), a constant volume averaged O density ($<n_O> = 1.2 \times 10^{16}$ m^{-3}) is assumed throughout the period in limiter configuration. For the specified prefill gas pressure of 0.5 mPa, this corresponds to ~5% of the H ions at full gas ionization. Since the prescribed DINA density is set to a target value $<n_e>/n_{GW}$ ~0.5 during the limiter phase, this constant $<n_O>$ provides a decreasing O concentration ($<c_O> = <n_O>/<n_e>$) up to X-point formation at t ~10 s (when I_p = 3.1 MA) – see Fig. 11b. Sensitivity studies show that the chosen value of $<n_O>$ in this particular example is ~85 % of the maximum allowed before radiation losses (from the O and sputtered W impurities) overcome P_{in}. The latter is given by the ohmic power and the specified ECH waveform starting at t ~4 s and rising linearly to ~2 MW by the end of the limiter phase. This ramp of central EC power is applied in an ad-hoc fashion under the assumption that some central EC will be required to inhibit core W accumulation (see Section 5.2) and to provide an

approximately constant rate dP_{in}/dt once the initial density rise has occurred, the rapid early peaks in $<c_W>$ and $<c_O>$ are passed and P_{ohm} saturates. This avoids further waves of W sputtering and edge radiative collapse which can lead to a contraction of the current channel and a rise in plasma self-inductance (and hence to MHD instabilities).

The O plays an important role in the W sputtering during the initial phase immediately after breakdown, with peak values of $<c_W>$ reached at t ~1.5 s. If $<n_O>$ is high enough, it even dominates over the W self-sputtering in the later stages, driving $T_{e,LCFS}$ down below the optimum for W sputtering since the system is now attracted to $<Y_{W-W}> = 1 - <Y_{O-W}>\Gamma_O/\Gamma_W$ rather than $<Y_{W-W}> = 1$. During the limiter phase in this example scenario, the inductive and resistive contributions to the poloidal magnetic flux consumption are respectively 38 Wb and 7 Wb (cf. 165 Wb and 26 Wb for the entire 65 s of current ramp-up) so that, in common with previous scenarios with a Be wall, resistive losses during this period, even with W, are not an important player in determining the available flattop duration.

Following the X-point transition, DINA has no W source model and, like $<n_e>$, $<c_W>$ is prescribed, usually assumed to vary linearly over 2 s from the end of the limiter phase to a fixed value during the divertor phase of the scenario (I_p ramp-up until t ~65 s, flattop and ramp-down to 1.6 MA); in the example of Fig. 11, $<c_W> = 3 \times 10^{-5}$ and $<n_e>/n_{GW}$ ~0.3. Such flattop values of $<c_W>$ are found to be reasonable from full integrated modelling (JINTRAC) of stationary 15 MA hydrogen L-mode plasmas at similar $<n_e>$ including realistic W source calculations from divertor and main wall interactions. During the current rise in divertor configuration, P_{ECH} is ramped linearly to ~14 MW in DINA and thereafter increased to the maximum available 40 MW during the flattop. The duration of the latter is ~170 s, limited by the maximum allowable current in the CS1 modules of the CS. Controlled current ramp-down requires a further 63 s. At the chosen value of flattop $<c_W>$, this scenario produces P_{SOL} ~35 MW, with P_{rad} ~7 MW, of which ~70% is due to W radiation. These kinds of values are a key input to the engineering design of the TFW to be installed for SRO (see Section 2) which is at the conceptual stage at the time of writing. Although DINA indicates the possibility of rather long plateau phases, the inertial wall will certainly limit the maximum flattop duration. At present the wall design target is set to ~30 s at full available heating power.

Whilst these initial DINA scoping studies with an improved limiter phase W source model do indicate that there will be a limit in allowable O concentration, the model simplicity is such, for example, that the absolute value of "dangerous" O concentration cannot be considered quantitatively predictable. Moreover, the DINA model lacks a realistic impurity core transport description, an issue which is being explored by the higher fidelity integrated modelling described in the following section. The DINA simulations do, however, capture the essential character of experimental experience – that it will always be a balance between increasing additional heating to increase core temperatures and overcome radiative losses, whilst at the same time avoiding too high an increase in $T_{e,LCFS}$ which leads to a higher W source.

Regarding the SOLPS-ITER limiter simulations, the initial database discussed here requires further improvement and wider parametric scans. In particular, exploration of the impact not just of the magnitude of the cross-field transport, but of radial transport profiles is required, as is the effect of prompt re-deposition and the presence of residual or deliberately seeded impurities. This work is underway and will be the subject of a forthcoming separate publication.

A final important point which can be made in the light of these SOLPS-ITER limiter configuration stationary modelling findings is that if the self-regulating mechanism identified by the simulations will really be operational during the early current ramp in ITER with a W FW, then the accompanying relatively high values of f_{rad} imply reduced P_{SOL} compared with the baseline assumptions which were previously employed to estimate heat flux densities on the Be FW panels during the inner wall limiter phase [1]. This will provide some welcome margin against the high heat loads which might otherwise have arisen with Be armour due longwave misalignments on the inner column and which imposed rather strict requirements on the FW panel alignment [1] in addition to the specific double logarithmic toroidal shaping designed to accommodate the presence on ITER of a possible narrow SOL parallel heat flux channel found in multi-machine studies of inner wall limited plasmas [93]. At present, the experiments recently performed on the EAST tokamak described below in Section 5.3 do tend to support the modelling SOLPS-ITER modelling conclusions. Further confirmation is awaited from other tokamaks operating with W main chamber PFCs.

5.2. JINTRAC limiter phase integrated modelling

As a complement to the SOLPS-ITER and DINA code simulations in Section 5.1, some first attempts have been made to perform integrated modelling of hydrogen HFS limiter plasmas with the JINTRAC code suite (used in COCONUT mode coupling the core and edge transport codes JETTO-SANCO and EDGE2D-EIRENE [95]). The specific aim is to include a realistic plasma and impurity transport model, but the JINTRAC simulations also have the advantage that time dependence can be included, though not yet for an evolving magnetic equilibrium. In fact, the possibility to perform limiter simulations with JINTRAC has been re-enabled for this ITER assessment on the basis of a new scheme in support of generalized grid geometries in EDGE2D-EIRENE. For the simulations described here, the JINTRAC edge grid has been converted from the SOLPS-ITER grid in Fig. 9a at $I_p = 2$ MA, $B_T = 5.3$ T.

In common with the SOLPS-ITER runs, the JINTRAC simulations include W (assuming no prompt re-deposition) but use a bundling scheme with 6 superstates. Both codes compute the W ionisation balance and radiation with ADAS [96] using the most recently made available data for W and assume a Mach = 1 sheath boundary condition at the limiter target (for each species individually).

Core turbulent transport is determined by TGLF-SAT2 [97], while neoclassical W transport is calculated with the NEO code [28]. Radial transport in the SOL is described with an assumption of a continuous exponential transition from heat and particle diffusivities and convection at the LCFS to fixed prescribed far-SOL diffusivities $\chi_{e,far\ SOL} = \chi_{i,far\ SOL} = 1.0\ m^2/s$, $D_{far\ SOL} = 0.3\ m^2/s$ and zero far-SOL convection [98]. Simulations are initialised at high density and then continued until stationary conditions are achieved. The time evolution of edge conditions in some of the scans is artificially slowed down in COCONUT due to the application of a core–edge partial coupling scheme in which EDGE2D-EIRENE is only advanced every 12th time step. This does not affect the stationary solution, which is typically achieved over timescales of ~25 s.

Two sets of simulations have been performed in this preliminary limiter phase integrated modelling effort. The first is a single scan in H puff rate in the range $1 - 4 \times 10^{19}\ s^{-1}$ at fixed $P_{ECH} = 3.3$ MW (the same value of P_{in} used for the reference SOLPS-ITER case in Fig. 9) with a prescribed Gaussian shaped EC deposition profile located at ρ ~0.2 in the core. This differs somewhat to the SOLPS-ITER runs, which use a simple uniform and much broader EC deposition profile. The results are in very reasonable quantitative agreement with the SOLPS-ITER simulations bearing in mind that the values of P_{in} (JINTRAC also includes an ohmic power contribution), gas puff strength etc. are not exactly matched. The same self-regulation of the edge heat flux is readily found in the integrated simulations with similar $<c_W>$ ~10^{-4}, f_{rad} ~0.85 (cf. Fig. 9b,c), $T_{e,LCFS}$ ~67 eV (cf. Fig. 10c) and $<Z_{W,LCFS}>$ ~12 to the reference SOLPS-ITER case. Despite the high radiation level, a consistent core–edge stationary solution can be achieved and is an indication that the risk of a continuously increasing core W accumulation and associated core plasma collapse is low, providing the heating and fuelling schemes are not abruptly changed.

Exploring the impact of EC power deposition location (from central to progressively off-axis heating) was the main objective of the second set of simulations in which the H gas puff rate is now fixed at $1.5 \times 10^{19}\ s^{-1}$, near the low end of the gas puff scan in the first set, giving $n_{e,LCFS}$

$\sim$1 x 10^{18} m^{-3}. The same $P_{ECH} = 3.3$ MW is applied but now with the EC heating and current drive calculated using the GRAY code [99], injecting O-mode beams at a power of 3.0 MW through an equatorial launcher with varying poloidal angle of 5.0–21.5°. The principal outcome of this simulation scan is that it is important to maintain centrally located EC heat deposition. If the deposition location is shifted outwards, beyond $\rho \sim 0.3$, the first-pass EC heat absorption fraction decreases significantly due to the lower T_e in the plasma periphery. Moreover, the change in core temperature profile gradients inside the EC deposition location drives an increase in inwards-directed neoclassical W transport, a situation which is further aggravated by a reduction in the predicted central turbulent W transport. Although stationary conditions can still be obtained if the EC beam is positioned at $\rho \lesssim 0.4$, the absorbed power is reduced to only about $\sim$1–1.5 MW in the simulation with EC deposition near $\rho = 0.45$. In this case, W starts to accumulate in the very core in a self-accelerating manner until the radiation becomes too large to prevent the formation of a hollow core temperature profile and finally the appearance of a current hole and radiative collapse in the centre. This behaviour may be enhanced by the reduced EC first-pass absorption efficiency, since the core temperature can be more easily affected by the strong core W radiation with reduced heat input, and the reflected power that has not been absorbed will be deposited mainly in the edge regions of the plasma and thus cannot contribute to the prevention of a core radiative collapse.

Fig. 12 illustrates some of the above features and shows how this core accumulation may be further accelerated in the case of an instantaneous change of the EC heat deposition. It compiles the results from just two of the time-dependent deposition scan simulations in which the EC power (Fig. 12a) is deposited initially centrally at $\rho_{EC,dep.} \sim 0.15$ in both cases, but is then, in the second simulation, instantaneously switched to very peripheral deposition at $\rho_{EC,dep.} \sim 0.55$ at $t = 0$ s (the deposition profile in this more off-axis extreme case is a prescribed Gaussian shape and not generated with GRAY). At this time, the heat from the new, more peripheral EC deposition, adds up in the edge to that already present from the stationary solution obtained previously with central EC heating. This produces a strong perturbation in SOL heat flux which in turn provokes a large increase in the W source (leading to accelerated W self-sputtering) and associated W flow into the core. The plasma temperature inside the deposition radius collapses (Fig. 12b), there is a very strong increase in the inward neoclassical W convection velocity (Fig. 12c) and radiative collapse at t $\sim$9 s (Fig. 12d). As discussed in the following section, this result, and those described earlier concerning self-regulation of the radiative fraction, closely resemble the behaviour seen in recent dedicated W limiter start-up experiments performed on EAST in support of the ITER re-baseline.

An interesting point to note in concluding this section is that the conditions of these ITER limiter plasmas are closer to those achievable in current devices, where neoclassical transport can dominate in the core regions because of higher collisionality and normalized toroidal rotation. In contrast, for ITER Q = 10 plasmas with strong alpha heating, anomalous rather than neoclassical transport dominates the W impurity dynamics in the central region (Section 3). This anomalous transport dominance at high Q means that increasing the W source would be expected to lead to a higher W edge/core density, but not to uncontrolled profile peaking. For the same reason, the core W peaking should not depend strongly on the level of EC power, which, if the core W radiation levels are too high in high Q plasmas, can simply be increased to offset the radiative loss and maintain fusion performance (but at the cost of decreasing Q see Fig. 2c and [10 11]). In contrast, for the limiter start-up plasmas, where neoclassical transport dominates over turbulent transport and W is driven into the core, central EC heating will almost certainly be required to control peaking of the W density profile.

5.3. Tungsten limiter start-up experiments on EAST

The two essential conclusions derived from the ITER modelling in the two previous sections: self-regulation of the W core concentration and the need for central EC power deposition when running plasmas on W limiters have both been demonstrated in dedicated experiments performed in the early part of 2024 on the EAST tokamak. These discharges were part of a special mini-campaign executed in support of the ITER re-baseline and concerned not just limiter start-up, but also boronization, ICWC and the impact of ELMs on main chamber W sources (see [11] for details of the ELM experiments).

Plasma start-up on EAST is predominantly on the Mo tiled inner column, so W limiter ramp-up tests cannot be performed in the same configuration ITER plans to use. However, EAST has recently installed a single, actively cooled, bulk W outer limiter centred on the OMP and consisting of 7 individual plasma-facing units (PFU) comprising chains of W monoblocks resembling closely the PFU arrangement of the ITER divertor targets (Fig. 13a).

The EAST outboard limiter blade is toroidally and poloidally shaped and the individual monoblocks are toroidally bevelled to hide leading edges as in the ITER divertor target design [13 100]. Start-up on this limiter in EAST had never been routinely attempted before the dedicated ITER re-baseline campaign, which aimed to try first to establish evidence for stationary self-regulation of W sputtering and second to investigate quantitively the impact of early W release on the subsequent development of the discharge current ramp-up, including the divertor phase. In fact, plasma position control issues for outboard start-up meant that only the first part of the programme could be executed, in addition to some important tests of the ECH deposition location. Fig. 13b, illustrates the typical outboard limited magnetic equilibrium finally used, together with the approximate EC deposition locations for the two beams deployed for core and off-axis heating.

Although the original experimental plan was to study a range of plasma current and density, the position control issues meant that the majority of useful discharges were executed at $I_p = 200$ kA ($B_T = 2.5$ T) and for a pair of densities such that $\overline{n}_e/n_{GW} \sim 0.15$ and 0.35 (where here $\overline{n}_e$ is the line averaged density). All pulses were run some days after a previous boronization (using carborane as opposed to the more common diborane process), but even a handful of the typical plasmas run on the outboard limiter were sufficient to essentially completely remove any B deposits in the main plasma interaction areas. The principal findings may be summarized by considering a small subset of just three discharges, for which the time traces of key plasma signals are compiled Fig. 14. A typical pulse has a flattop duration on the W outer limiter of $\sim$4 s, far longer than the rather short HFS limiter ramp-up phases which are typically used in normal diverted discharges ($\sim$0.5 s), and easily long enough to establish stationary conditions with respect to all relevant timescales.

All pulses used a single 140 GHz gyrotron ($P_{ECH} \sim 0.65$ MW) heating centrally in 2^{nd} harmonic X-mode from the discharge onset (EC2 in Fig. 14e). This EC assist was used to ensure success of the plasmas starting on W, but no significant effort was invested to try and establish plasma without it in view of priority given to studying stationary discharges. (In fact High Frequency GDC (HF-GDC) [101] was also used for breakdown assist in the discharges, but separate tests conducted after the limiter start-up experiments showed no differences if the HF-GDC is removed.) It should not therefore be concluded from these experiments that EC breakdown and burn-through assist is mandatory for plasma start-up on W in EAST, although current ramp-up attempts on the HFS Mo limiter were systematically unsuccessful when ECH was not applied at start-up. Indeed, ASDEX Upgrade has in the past run several experimental campaigns with non-boronized W coated main chamber walls and routinely achieved ohmic current ramp-up on W [88,102]. From the start of operations ITER will be equipped with a 170 GHz EC system permitting pre-ionization and heating during burn-through (2^{nd} harmonic X-mode for $B_T = 2.65$ T or 1^{st} harmonic O-mode at $B_T = 2.65$ T) [103].

In the three example pulses of Fig. 14, two (#132749 and #132773) are at the lowest density ($\overline{n}_e/n_{GW} \sim 0.15$), with the third (#132759) at

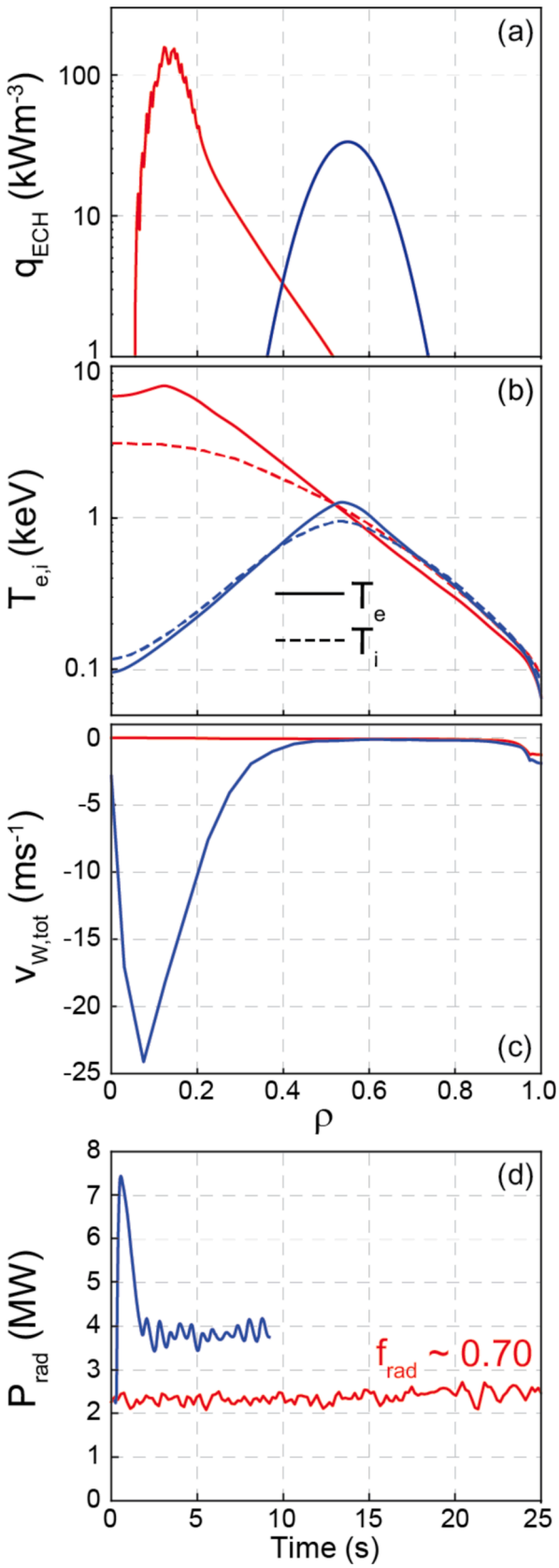

(caption on next column)

Fig. 12. Selected output from time-dependent JINTRAC COCONUT code runs for ITER limiter phase plasmas for two examples in which EC deposition is either maintained on-axis (red curves) or instantaneously switched from central to far off-axis (blue curves) at t = 0. The numerical grid is generated from the same I_p = 2 MA, B_T = 5.3 T DINA equilibrium as for the SOLPS-ITER stationary simulations (Fig. 9a). For the two cases of on (red) and off-axis (blue) EC power deposition, profiles of (a) EC heat deposition to electrons; (b) T_e, T_i, (c) neo-classical W convection velocities. In (d) the time traces of total radiation for the two EC deposition cases showing how the off-axis heated discharge terminates early due to strong core W accumulation and core temperature collapse inside the deposition radius. (For interpretation of the references to colour in this figure legend, the reader is referred to the web version of this article.)

roughly twice this lowest value (Fig. 14b). As might be expected with central ECH power, core T_e profiles (not shown) are rather peaked and can reach ~6 keV and ~1.5 keV for the low and high density plasma targets respectively (the range of values is very consistent with those reported more than a decade ago from ASDEX Upgrade for HFS limiter plasmas on W with similar plasma parameters and EC heating [102]). At the plasma boundary, fast reciprocating Langmuir probe data indicates $T_{e,LCFS}$ ~30 eV and ~10 eV for the low and high density pulses.

An important observation is that the total radiated power (Fig. 14g) eventually saturates at both densities to the same value of ~0.4 MW, corresponding to f_{rad} ~0.6. This is strongly indicative of the self-regulating sputtering mechanism seen in the SOLPS-ITER boundary modelling for ITER described in Section 5.1, though the fact that P_{rad} tends to the same value independent of density is not at all obvious given that the available core (EUV) spectroscopy (not shown) reveals that there is a very large variety of impurity species in these EAST limiter plasmas. Emission is found from the lighter impurities (B, C, O, N) and from high charge states of heavier species (Fe, Cu, Mo, W). The former originate mostly as residues from the carborane boronization processes applied prior to these experiments, from small leaks and possibly from previous experiments using N-seeding. The heavier species come from the Mo central column tiles, the W outer limiter and from various in-vessel components (steel structures, RF/LH antenna Faraday screens etc.). Unfortunately, it is not yet possible to transform these core line emission signals into absolute concentrations.

It is clear, however, that even the lower measured values of $T_{e,LCFS}$ would be easily sufficient to provide for W self-sputtering, or sputtering by other impurities, particularly due to the higher ionization states formed deep in the core, returning to the limiter as highly charged ions and being accelerated through the sheath potential. Comparing any given species, there is a trend in the spectroscopy data for the heavier impurity emission to decrease with increasing density, consistent with a reduced edge source, as would be expected for lower $T_{e,LCFS}$. Unfortunately, since the source strength cannot yet be quantified with the existing data, boundary modelling of these discharges will be challenging. Concerning the observation of constant f_{rad} independent of density (Fig. 14g), this would indeed be one of the expected consequences of the strong self-regulation mechanism discussed in Section 5.1 in the context of the SOLPS-ITER modelling. Nevertheless, further experiments and analysis are required to provide a wider range of plasma conditions and some quantitative estimates of the impurity source rates and core concentrations.

A second key result for future ITER operation is evident from pulse #132749 in which, just before t = 3 s, the standard central heating gyrotron is switched off and replaced by a second beam (EC4) heating far off-axis at ρ ~0.6 (Fig. 14f). The plasma disrupts almost immediately (this is a reproducible observation). The signals are not shown here, but this is accompanied by very strong off-axis peaking of the T_e profile, a strong rise in edge density and an increase in peak surface temperature at the W limiter (measured by IR thermography). This latter temperature rise may be a consequence of a sharp increase in EC heat deposition in the periphery as seen in the JINTRAC modelling for ITER described in Section 5.2.

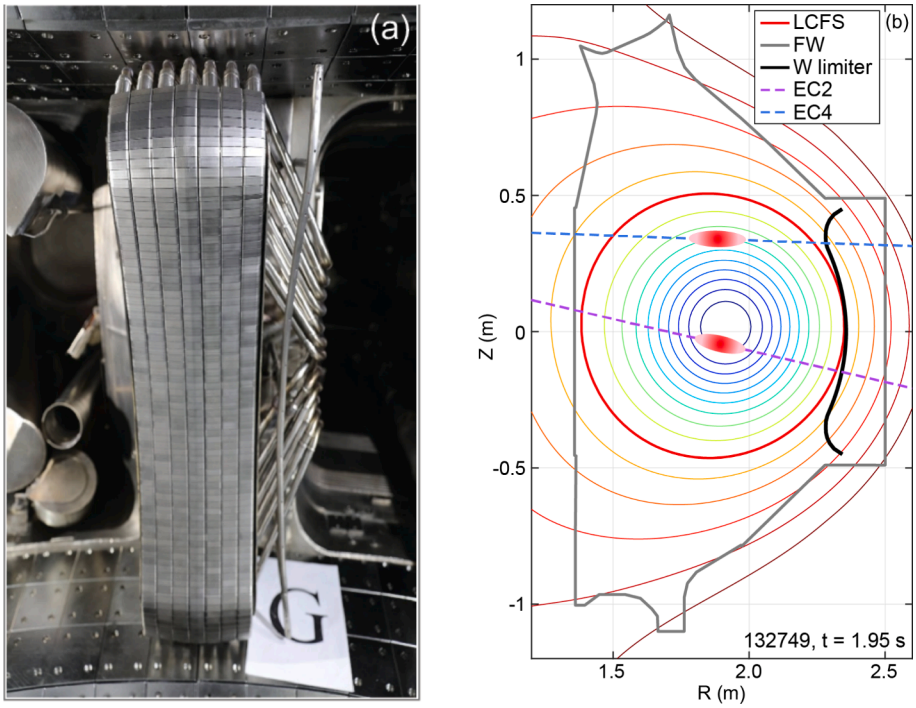

Fig. 13. (a) Photograph at pre-installation of the EAST actively cooled poloidally and toroidally shaped outer poloidal W limiter, comprising 7 PFUs with toroidally bevelled monoblocks very similar to the design of the ITER divertor vertical targets [13,100]; (b) Poloidal cross-section showing the magnetic equilibrium of the typical outer limiter circular plasma used in the EAST start-up experiments with locations of central and off-axis EC deposition.

Data analysis and modelling is still required to confirm the relative contribution of W accumulation and MHD as causes of the disruption, but this EAST experiment makes clear at least that if EC heating is required during W limiter phases, then it should be deposited centrally. As mentioned earlier, that central heating is required to prevent core W accumulation in the divertor phases of tokamak plasmas with W PFCs has long been known (see e.g. [87]). However, the result from EAST is a direct (and probably the first) demonstration that the same very likely applies in the limiter phase and, moreover, that EC power may well be required in ITER, not only for breakdown assist but also during the early limiter ramp-up phase on W surfaces. These observations are generally in very good qualitative agreement with the JINTRAC results of Section 5.2.

At the time of writing, the plasma position and shape control issues which impacted these first EAST experiments have now been resolved, so the full originally intended programme can be revisited. At the same time, very similar experiments are planned on the ASDEX Upgrade and WEST tokamaks (including start-up without prior boronization) to provide a healthy new database of W limiter start-up observations in support of the ITER studies. It should also be noted that studies of outboard W limiter plasmas were conducted on ASDEX Upgrade long before these new EAST experiments [104]. There, however, the focus was on the transient current ramp down phase on W coated graphite limiters with emphasis on modelling the migration of W eroded from the limiters in this phase (using DIVIMP impurity transport simulations on a fixed plasma background provided by SOLPS modelling). There is insufficient experimental data provided in [104] to assess the radiative fractions etc., but it is certainly clear that these transient limiter phases dominate the gross influx of neutral W.

6. Tungsten FW damage under disruption transients

Disruptions and vertical displacement event (VDE) induced heat loads have a major impact on the PFC lifetime and are one of the principal drivers of the need for an effective DMS. It is therefore essential to avoid, as far as possible, unmitigated disruptions and to commission the DMS as soon as possible in the IRP to ensure effective mitigation before operation with high plasma current and energy is attempted. A substantial fraction of the operational time in the new SRO phase of the re-baseline is dedicated to disruption load characterisation and mitigation.

Effective disruption mitigation needs to simultaneously meet the requirements for mitigation of the thermal quench (TQ), CQ and RE loads, where the TQ and CQ are considered as "thermal plasma loads" in the sense of being deposited on the material surface only (and not in the bulk). However, the specific choice for material injection which maximizes the mitigation of one load can lead to an increase in the other, especially RE production [105]. Runaways are of particular concern since they can potentially cause single event failure of PFCs through damage to the cooling interface, leading possibly to water leaks. Such eventualities present potential accident scenarios on ITER and come at an extremely high price in terms of cost and time to repair. The specific questions of CQ thermal loading and RE impact are considered in more detail in the following sections.

6.1. Current quench thermal loads

Regarding the TQ and CQ heat loads, the high melting point of W opens up a wider operational space than Be in terms of the range of I_p and plasma stored energy, W_{plasma} within which melting is avoided. The switch to W essentially eliminates unmitigated TQ-induced FW melting for Major Disruptions (MD), even at the highest stored energies (though this is still an issue for the divertor [106]). There remain issues, however, for the unmitigated VDE-induced TQ, where the plasma is in limiter configuration at the quench and can lead to W melting even for comparatively low stored energies (~20 MJ). Such events are, though, much more unlikely since they are expected to occur 100–200 ms after VDE detection [107] and there should thus be ample time for mitigation.

In the case of Be, a detailed analysis (using the DINA [91]-SMITER [108]-MEMOS-U [109] code workflow) of the CQ-induced loads for the worst case VDEs and MDs (at $I_p = 15$ MA) found severe melting and melt motion on upper FW panels during upwards going events, and to a lesser extent on the lower, outer rows for downward quenches [110]. The same

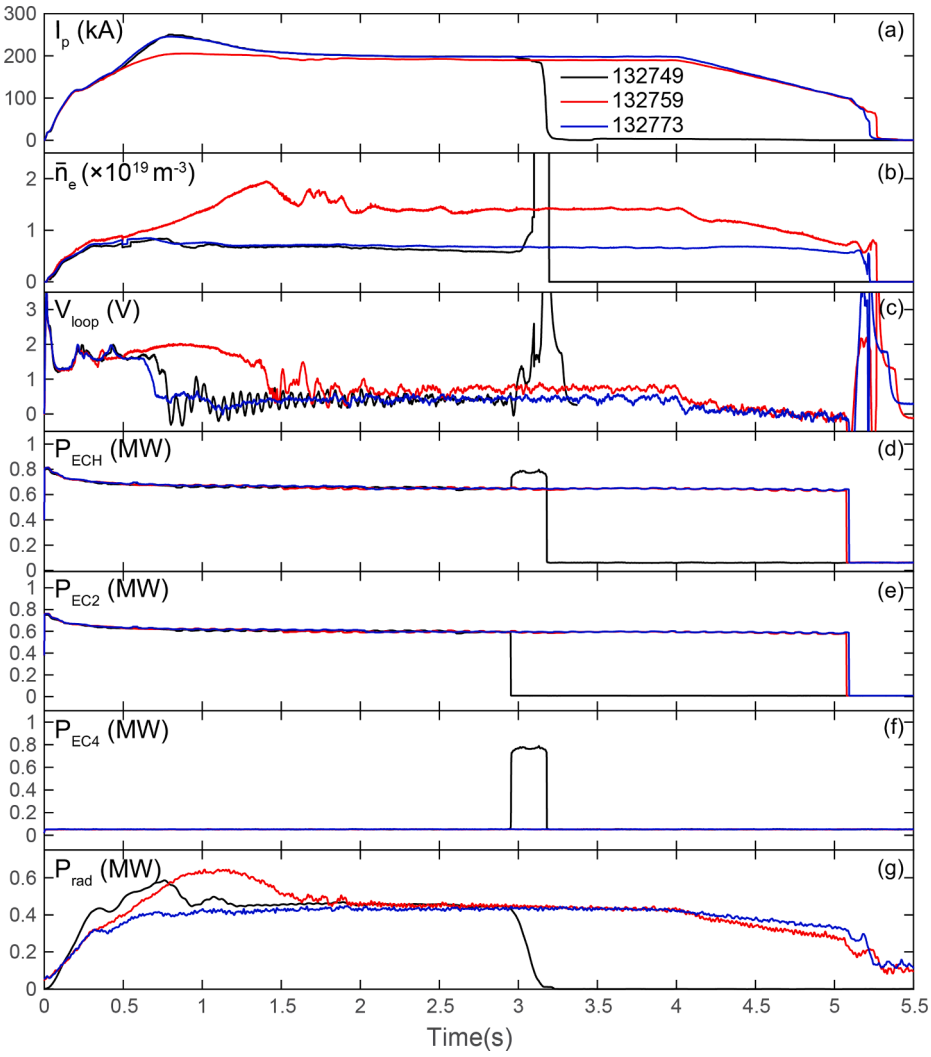

Fig. 14. Summary of key time traces for a set of three EAST outboard deuterium W limiter plasmas at (a) I_p = 200 kA and two densities (b) with $\bar{n}_e/n_{GW}$ ~0.15 and ~0.35. The ECH powers (d) P_{EC2} and (e) P_{EC4} refer to the deposition locations in Fig. 13b. Note the low electric field (~0.12 Vm^{-1}, (c)) in the early start-up phase (EAST major radius, R = 1.85 m) and the tendency in (g) for P_{rad} to saturate at a fixed value independent of density.

workflow applied to W armour predicts that surface melting will still occur on the upper panels under worst case conditions for upward going quenches at 15 MA, but is absent on the lower panels for downward events. Scaling the poloidal field magnetic energy and CQ time with plasma current ($\tau_{CQ} \propto I_p^{1/2}$, $W_{mag} \propto I_p^2$) [106], melting on W upper FW panels is predicted to begin for I_p ~11–12 MA. In [110], fairly substantial melting occurs on Be already at I_p = 7.5 MA.

The MEMOS-U calculations for the worst case CQ on W find maximum erosion depths of ~0.4 mm, a factor of ~7 lower than for Be under the same loads, which is a major gain with regard to the ability of FW panels to tolerate a limited number of events. Whilst the principal reason for the reduced erosion depth is the much higher melt temperature of W, it is also in part due to the modified melt motion, where, in the case of W, Lorentz forces on the melt layer are driven by thermionic electron current emission from the heated surface (typically dominating) and the halo current carrying the heat flux. For Be, thermionic emission is essentially absent, and the melt motion is determined only by the halo current.

For both materials, once melting and melt motion occurs, the melt displacement will easily be sufficient for the melt layer to bridge over some of the toroidal gaps (typical gap width ~1 mm) between poloidally adjacent fingers making up any given FW panel. Such behaviour has already clearly been observed on the JET Be upper dump tiles under upward going CQ loads [111] and has been well reproduced in MEMOS-U modelling [112]. If this bridging also leads to gap filling such that fingers are electrically connected, and depending on where this takes place, significant eddy currents can circulate in the panels even for follow-up disruptions whose CQ has been mitigated. The associated electromagnetic forces can be very large and could potentially lead to mechanical failure of the panels in single events.

An outstanding question is thus whether this gap filling will occur on ITER with W PFCs. Gap wetting is a complex process and is sensitive to melt speed, pool depth, lifetime and the liquid metal and wall temperatures. Experiments designed specifically to address gap bridging and infiltration for W material have been performed quite recently on ASDEX Upgrade [113]. Under the conditions of this experiment (repeated ELM-induced transient melting on specially engineered samples exposed in the outer divertor), re-solidification limited wetting and weak attachment of resolidified melt were observed (and confirmed by melt modelling), including the wetting of inner gap walls (thus no gap infiltration). This is a consequence of re-solidification, which prevents the melt from revolving around the corners by modification of the sharp edge topology. A second dedicated experiment on bridging vs. infiltration has just been executed on WEST, revealing a similar picture to that found in ASDEX Upgrade despite the different scenario (sustained melt pool due to steady state loads).

Returning to the modelling of macroscopic CQ-induced melting on the ITER FW panels [110], the MEMOS-U code enables unique calculations accounting for melt motion. This allows an assessment of the damage in terms of permanent deformations of the surface topology [110,112] and of material losses due to splashing [114], in contrast to the melt thickness which by itself carries limited information given that the melt eventually resolidifies. Since the MEMOS-U physics model addresses heat transfer in PFCs and the macroscopic motion of the formed melt pools, heat flux loading constitutes an external input to the code. Thus, MEMOS-U can simulate CQ-induced melting with heat flux input accounting both for the 3D nature of the plasma wetted area and the time varying magnetic equilibrium of the quenching plasma (based for the simulations discussed here on DINA DS code simulations of the CQ phase), but the process of vapour shielding (VS) can only be introduced externally. Such an attempt was made in the Be melt modelling of [110], within an approximation based on shielding coefficients derived from 1D3V Particle-in-Cell simulations with the PIXI code [115]. These coefficients are not yet available for W.

For the worst case 15 MA upward going VDE CQ studied in [110] ($\tau_{CQ} = 400$ ms, $n_{Be} = 1x10^{19}$ m^{-3}), the reduction in eroded depth due to Be vapour shielding varied over the wetted area by a factor of 1.5–2, with reduction of the maximum erosion value from ~3 mm to ~2 mm. The melt thickness variations between shielded and unshielded cases were 10–30 %, with the values in the shielded case within the range of 200–500 μm over most of the wetted area [114].

To explore the 2D nature of the shield dynamics, new simulations have been performed with the TOKES code [116], which includes a VS model reasonably well benchmarked against very short duration transients [117] and which operates in 2D. Unlike the MEMOS-U simulations, which adopt the spatio-temporal varying heat flux as an input, TOKES cannot yet follow the CQ equilibrium evolution and, given the 2D nature, is unable to account for the reduced wetted areas for heat loads introduced by the 3D FW panel shaping. For the same upward going DINA DS CQ simulations adopted by the MEMOS-U studies, it thus assumes that the equilibrium is fixed in time from the first point at which significant heat flux is deposited in limiter configuration on the upper FW panels. Thereafter, the TOKES model assumes (extremely conservatively) that the total magnetic energy which should be dissipated during the CQ is stored as ion thermal energy in the core and is then transferred to the electrons via equipartition, at a rate which is adjusted to provide appropriate low electron temperatures in the halo region and which fits the DINA value of τ_{CQ}.

The OMP λ_q of the halo is approximately matched to the values used in [110] by adjusting radial plasma transport coefficients. Simulations have been performed with and without VS, for varying λ_q, E_{CQ} and τ_{CQ} (corresponding to I_p = 7.5, 10.0, 12.5 and 15 MA) with the latter two quantities varied using the same scalings mentioned above. Details may be found in [106]. Fig. 15 summarizes a selection of results for a 15 MA

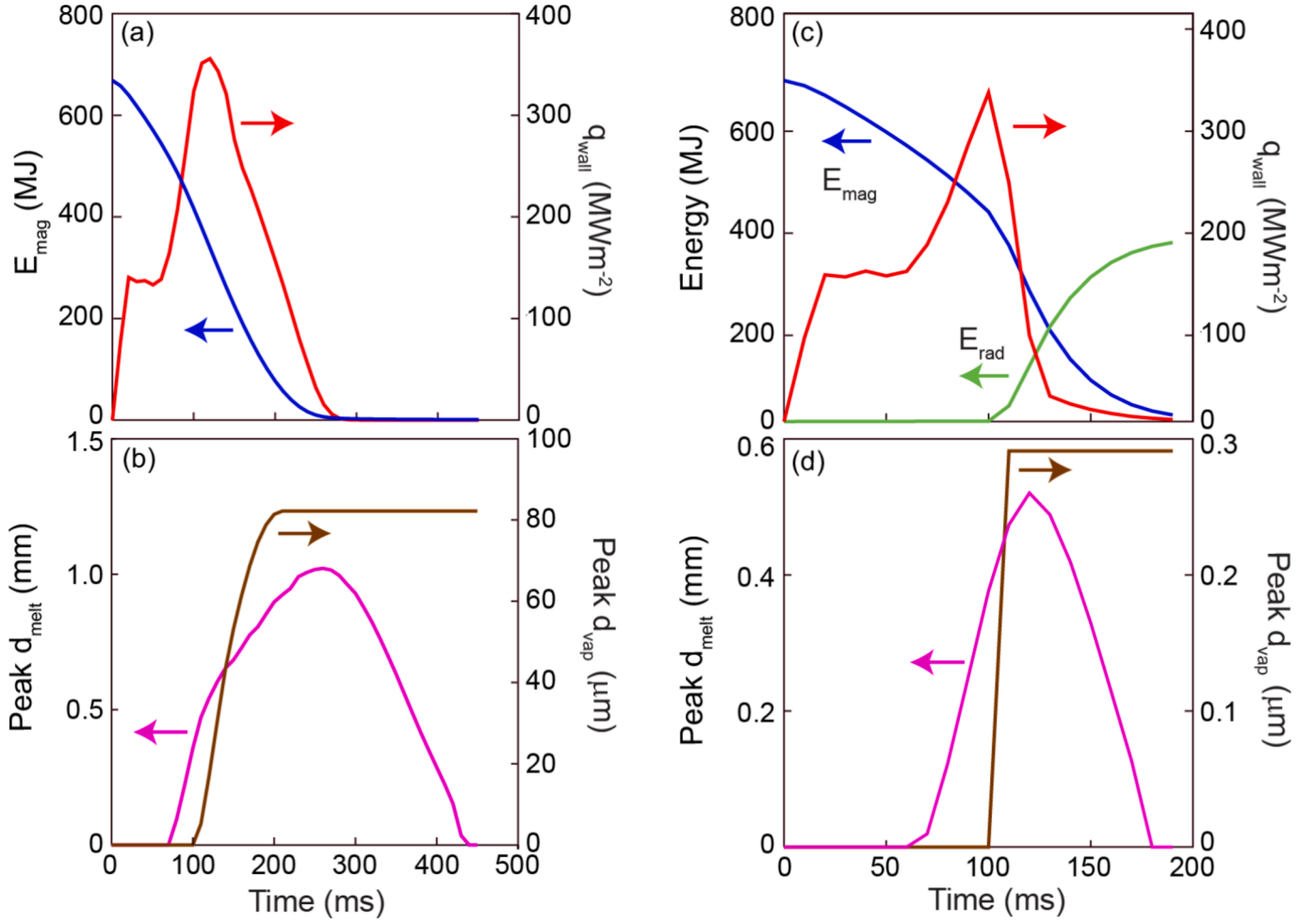

Fig. 15. Compilation of results from TOKES simulations for W armour with and without vapour shielding for one of the upward going 15 MA worst case VDE current quenches studied with the MEMOS-U melt code for the case of a Be FW in [110]: (a) and (c) time variation of the wall heat flux (q_{wall}) and magnetic (E_{mag}) and radiated (E_{rad}) energies without (a) and with (c) vapour shielding; (b) and (d) peak W melt and vaporization depths respectively without and with shielding. E_{CQ} = 670 MJ, τ_{CQ} = 250 ms, λ_q = 3.5 cm. The simulations are carried through to complete re-solidification. Note the timescale differences between the cases with and without VS. Curves are extracted from [106].

upward going VDE or MD CQ with $E_{mag} = 670$ MJ, $\tau_{CQ} = 250$ ms, $\lambda_q = 3.5$ cm.

Vapour shielding reduces the peak melt depth, d_{melt} by ~factor 2, the vaporization depth, d_{vap} by more than 2 orders of magnitude, the melt duration by nearly a factor 3 (this also significantly decreases the time over which melt motion can occur) and ~50 % of the magnetic energy is radiated by the vapour shield near the FW panels. An important contributor to the reduction in heat loads to the FW panel surface with shielding on is the rapid filling, shortly after intense vaporization begins, of the entire halo region with W plasma, radiating the magnetic field energy over a large FW area at comparatively low power density.

As I_p is decreased in the simulations, the shield strength is drastically reduced because the vaporization flux decreases significantly. Vaporization becomes important only for the 12.5 MA simulation, and in this case only ~14 % of E_{mag} is radiated. Tungsten melting still occurs at $I_p =$ 10 MA, with a peak d_{melt} ~0.4 mm and a melt duration of ~160 ms, comparable to the 15 MA worst case with shielding. No melting is found at 7.5 MA. An important conclusion is therefore that, given the current limitations of the TOKES model (i.e. that 3D effects and the proper time dependence cannot be included) unmitigated CQs at lower I_p on W can generate similar melting and melt durations to events at the highest current, where shielding is effective.

Concerning the relative performance of Be and W under these heavy unmitigated CQ transients, the TOKES study in [106] (from which the curves in Fig. 15 are extracted) found relatively small overall differences between the two armour choices for the same input heat flux waveform. This may at first seem surprising given that W is a much stronger radiator than Be. However, the much higher quantity of vapour in the case of Be compared to W, and the point at which vaporization begins, are key factors. For Be, vaporization starts early (due to the much lower vaporization temperature compared with W) when the majority of E_{mag} has yet to be dissipated. For W, vaporization starts much later, when a substantial fraction of E_{mag} has been exhausted in the halo and an order of magnitude fewer atoms are vaporized. This large difference in vaporized quantity and the later vaporization onset lead to similar overall peak d_{melt} and melt duration between the two materials.

It is important to point out that all of the unmitigated disruption melt calculations performed to date (thus using MEMOS-U and TOKES) must be considered only approximate given their reliance on the 2D DINA DS disruption simulations. In reality, the CQ phase is expected to be an extremely variable spatio-temporal event, with significant MHD activity and a complex 3D heat deposition pattern with strong filamentary nature [107]. The assumption of a 2D equilibrium with an essentially smooth envelope of energy deposition, leading to global surface melting with well-defined wetted area, will thus likely be a rather conservative picture. More realistic time and spatial heat deposition patterns are starting to become available through new 3D JOREK simulations and will eventually be used as input to more refined melt estimates.

6.2. Runaway electron impact

Of all transient loads, REs are the most serious concern for PFC damage on ITER. This is a consequence of the distinct nature of the runaway impact: potentially small impact areas, very fast timescales and deeper penetration into the material bulk than for normal thermal plasma transient loads which are deposited on the surfaces of components (e.g. due to ELMs or the disruption TQ and CQ). Runaway currents of up to $I_{RE} = 10$ MA could form in ITER carrying a kinetic energy of ~20 MJ, but the high fraction of magnetic energy stored in the poloidal field of this current means that a significant portion can be converted into kinetic energy depending on the timescale of the runaway loss [118].

The modelling strategy has been long established [119] and constitutes a two-step approach in which simulations of volumetric energy deposition of impacting REs by a Monte Carlo transport code provide the loading profile input for simulations of the PFC response e.g. by finite element modelling [120,121,122,123,124]. All such modelling has thus far been limited to the PFC thermal response, whilst the mechanical response in the solid phase and the hydrodynamic motion in the liquid phase have not yet been considered. The development of more realistic physics models has been hindered by the absence of dedicated, specially designed experiments since uncontrolled damage observations, e.g. [125,126,127,128] cannot provide sufficiently detailed input concerning loading in terms of wetted area, RE impact characteristics and, crucially, energy absorbed.

Deliberate RE generation experiments on JET (using massive gas injection to form a RE beam) have already demonstrated the appreciable damage which can be caused on Be PFCs by short duration RE impact [125 128]. These experiments concerned RE interaction with bulk Be inner wall guard limiters with similar apex-like design to the ITER FW panel geometry. They have been modelled at IO using a workflow comprising the SMITER field line tracer [108], the GEANT4 [129] (opensource Monte Carlo toolkit for simulating the passage of particles through matter) and the MEMOS-U [109] codes, with reasonable agreement found for the final damage profile, albeit subject to uncertainties due to ambiguities in the input assumptions concerning the RE beam parameters [130]. In fact, the incident transient which is qualitatively consistent with this post-mortem damage, with the (sparse) available JET plasma measurements during the RE event, and with the predicted 3D interaction zone (from field line tracing using the reconstructed CQ magnetic equilibrium), is that of a radially outward drifting beam with a very narrow energy deposition channel width ($\Delta_{RE} = 1 - 2$ mm), depositing $\lesssim$ 100 kJ over a time Δt_{RE} ~6 ms and composed of electrons with mean energy ~13 MeV impacting the Be tile surface at roughly the field line incidence (pitch) angle deduced from the field line trace.

Encouraged by the reasonable agreement found in the JET benchmarking exercise, the same workflow was applied in [130] to a proxy case on ITER (pre-dating the re-baseline and thus considering Be FW panels) in which the RE impact was assumed to occur according to similar dynamics during the worst case upward going VDE CQ discussed in Section 6.1. Unsurprisingly, given the real experimental damage already seen on JET at comparatively low deposited RE energies compared to what could occur on ITER, the study concluded that bulk melting, with possible temperature excursions at the cooling channel interface above recommended thresholds, could occur already at very low I_p (~few MA), depending on how many FW panels are impacted in a single event. This potential threat to cooling channel integrity when RE mitigation/avoidance strategies using the DMS are being first tested, is the principal driver in the re-baseline for experiments to begin on a temporary, uncooled FW.

In support of the re-baseline, the in-house SMITER-GEANT4-MEMOS-U assessment for RE impact on Be has been repeated for W, but now with much higher fidelity in the GEANT4 simulations and with MEMOS-U replaced by a new melt code, MEMENTO (MEtallic Melt Evolution in Next-step TOkamaks) which incorporates all of the physics included in MEMOS-U, but within a modern computational framework, including non-uniform and adaptive meshing and parallelization [131 132]. Although the input configuration and main results from these new simulations are summarised below, there are many more details than can be included here. They will be the subject of a forthcoming publication.

Fig. 16 summarizes pictorially the assumed worst case and very simplified scenario, in which a runaway beam is supposed to destabilize during the upward going CQ at the point at which $q_{95} = 2$ is reached in a DINA DS simulation with RE generation and full conversion of the magnetic energy in the runaway plasma into RE energy (starting from a pre-disruptive plasma at $I_p = 15$ MA). At this point, I_{RE} ~9 MA and the RE beam intersects FW panel #8 at the top of the main chamber. In the 2016 Baseline, this is an Enhanced Heat Flux Be panel with hypervapotron cooling channels [133], a design which will be largely preserved for the new DT-1 W FW but which is not currently finalised.

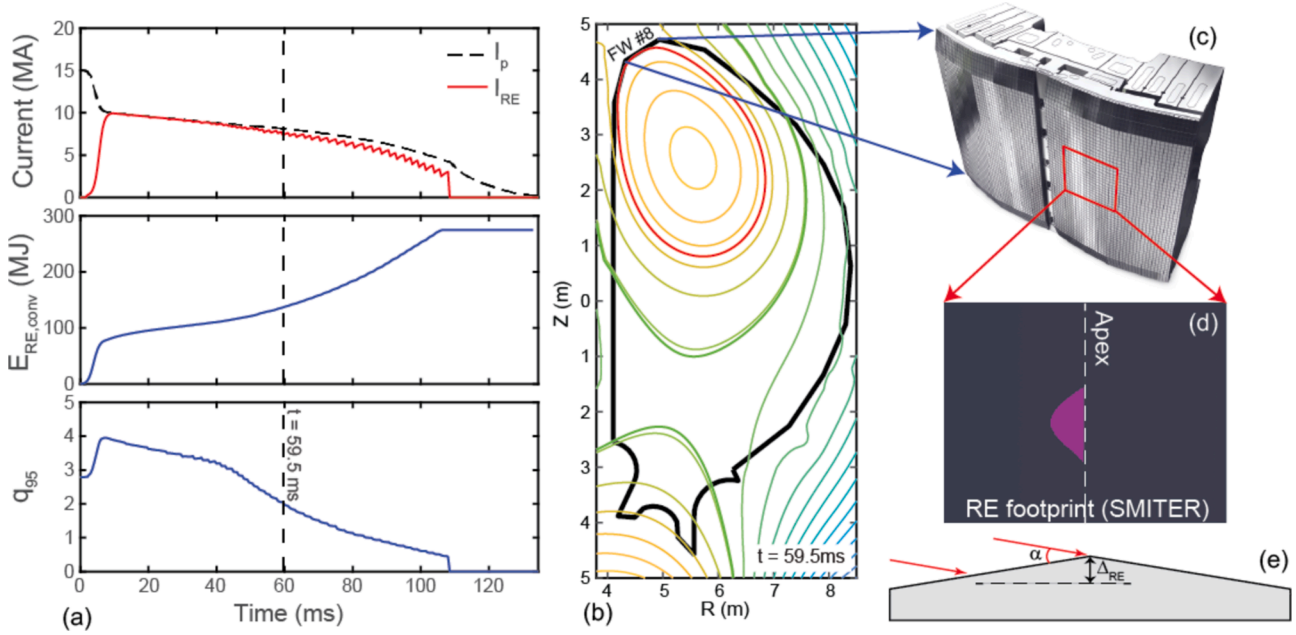

Fig. 16. Composite describing the key input parameters for the new RE impact simulations performed with the DINA-SMITER-GEANT4-MEMENTO code workflow: (a) DINA DS simulation (IMAS database shot 100097, run 1) including RE conversion during an upward going CQ at 15 MA, 5.3 T showing the runaway current and magnetic energy conversion with $q_{95} = 2$ reached at t = 59.5 ms; (b) magnetic equilibrium at $q_{95} = 2$ assumed as the instant at which the RE beam is destabilized with impact on FW panel #8; (c) Blanket Module CAD model illustrating the double winged apex structure of the FW panel; (d) SMITER field line tracing calculation of the RE beam wetted area for $\Delta_{RE} = 4$ mm; (e) schematic representation of the FW panel apex modelled as a simple rooftop with given fixed RE beam impact angle.

The runaways are assumed to deposit energy in a well-defined beam with width $\Delta_{RE} = 4$ mm, fixed essentially by the Larmor radius of electrons described by an energy distribution of the form f(E) ~exp(E/E_0), with $E_0 = 15$ MeV and E in the range 1 – 50 MeV. The RE impact area is obtained from 3D field line tracing (SMITER code) using the $q_{95} = 2$ equilibrium and accounting for the FW panel geometry. Energy deposition times are fixed in this extremely simplified description at 1 ms and 100 ms, representing respectively a case in which RE deposition is only kinetic, without conversion of magnetic energy, and the situation in which the beam is preserved for a much longer duration, allowing for some magnetic energy to be converted to RE kinetic energy. The amount of energy scales approximately with I_p in the first case and with I_p^2 in the second. All electrons are assumed to impact with the same grazing incidence angle of 5° (thus zero pitch angle) obtained from the field line trace, representing a further strong simplification.

The more refined GEANT4-MEMENTO simulations improve on the initial estimates made for RE loading on Be in [130] in several ways. Concerning first the use of GEANT4, a number of improvements have been made: (i) the most accurate electromagnetic libraries and scattering implementations are included (benchmarked for W); (ii) the magnetic field is taken into account for all charged products of the electromagnetic shower in the interior (primary electrons and secondary electrons/positrons) and the exterior of the material (scattered electrons/positrons); (iii) the spatial resolution is optimized, taking a small fraction of the W depth range of the least energetic REs (1 MeV) to ensure that the profile of the volumetric deposition is adequately resolved and (iv) the trade-off between the computational cost and the statistical Monte Carlo error bars is carefully controlled through a two-step approach combining uniformly distributed particle source loading of the entire wetted area (low statistics) with moving single-point particle source loading of the most affected region within the RE wetted area (high statistics).

Regarding the MEMENTO simulations, an improved model is used for the real panel geometry which includes the CuCrZr layer at the cooling interface, the hypervapotron shape, the convective cooling flux at the interface and the moving free surface due to vaporization. The field is set at 7 T, consistent with the location of FW panel #8 for the nominal $B_T = 5.3$ T. All cases discussed here assume an 8 mm W armour thickness (as it was for the previously modelled Be case).

Following exploration tests including the MEMENTO thermal transfer, a resolution of 20 μm has been chosen within the first 1 mm of material for the GEANT4 energy deposition simulations. Thereafter, the numerical grid resolution is relaxed. Even though the RE impacts in this very simple loading case are uniformly distributed (within the localised wetted region shown in Fig. 16), the 3D panel and magnetic field geometry, together with the fact that electrons scattered out of the material return to the surface under the action of the B-field, mean that the energy deposition is not uniform. From the ratio of the energy deposited over the apex to that over the most loaded region, the normalization for the single 'worst case' tile may be deduced (recalling that the panel design in the high flux areas occupied by FW panel #8 is a castellated structure made up of many small flat tiles (see Fig. 16c and [133])). This single "tile" (of surface area ~15 x 15 mm^2) is modelled thermally as 8 mm of W, 7 mm of CuCrZr heat sink and with boundary conditions as follows: thermally insulated sides facing the castellation gaps, vaporization and thermal radiation cooling from the free surface, and convection cooling flux at the CuCrZr-coolant interface.

A selection of the thermal transfer results obtained so far from the point of view of input to the FW design and the consequences for severe RE impact is compiled in Fig. 17 (three energy loads at 1 ms duration ($E_{RE} = 50$, 75 and 150 kJ) and two at 100 ms ($E_{RE} = 50$ and 200 kJ)). The key issues are the distribution of temperature through the armour thickness (Fig. 17a) and the values reached at the cooling interface for given total energy deposition (Fig. 17b). Table 1 provides more numerical information on the peak surface temperature, peak melt depth and erosion (due to vaporization) and temperature at the cooling interface for the different energy loads and loading durations.

As shown in Fig. 17a, enormous temperatures, exceeding 10,000 K, can easily be reached just below the surface if the total energy injected is incident over a short time. This is because most of the energy is deposited in a very shallow layer for this grazing incidence approximation. Although the MEMENTO code employs state-of-the-art values

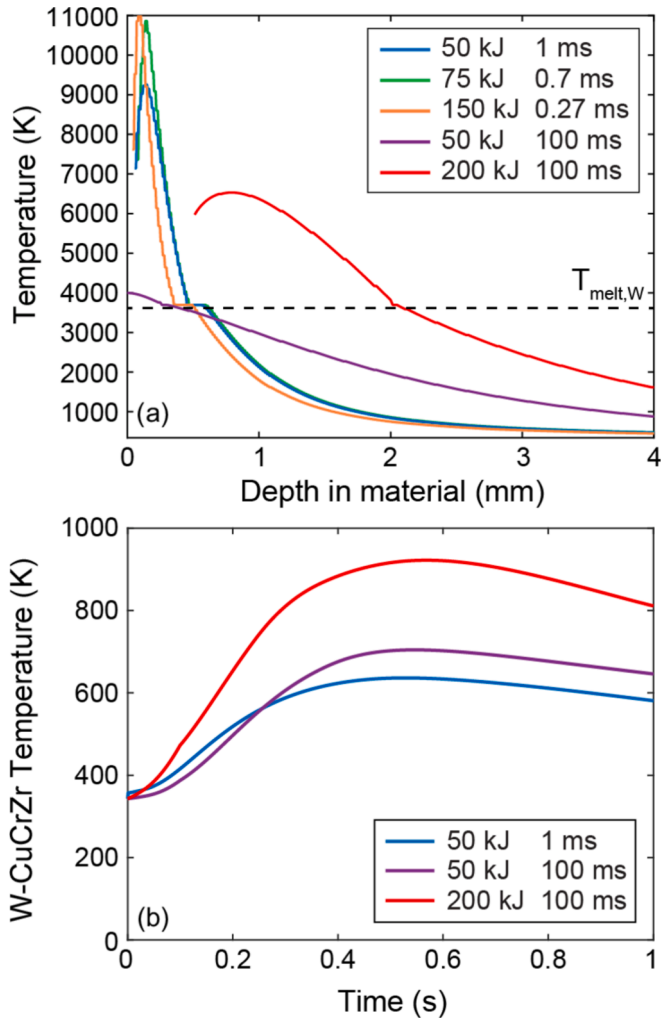

Fig. 17. Selected results from MEMENTO code modelling of a small (~15 mm x 15 mm), most loaded region near the apex on an ITER W FW panel under impact of a RE beam with the characteristics described in Fig. 16: (a) depth profiles of temperature for different RE energy deposition and loading times; (b) temperature evolution at the W-CuCrZr bond interface for three selected loading scenarios.

Table 1
Summary of MEMENTO code thermal calculations for different total RE energy loads at fixed energy deposition times of 1 ms and 100 ms (see also Fig. 17). Note that the values of maximum T_{surf} are given right at the surfaces and are lower than the peak temperatures in the material bulk, just below the surface.

Energy loaded	Over 1 ms			Over 100 ms	
	50 kJ	75 kJ *	150 kJ *	50 kJ	200 kJ
Max. T_{surf} (K)	7146	7361	7600	3995	5972
Max. d_{melt} (mm)	0.46 @ 1.8 ms	0.40	0.31	0.25 @ 100 ms	1.5 @ 114 ms
Erosion (μm)	93	67	31	0	540
Max. T at W – CuCrZr (K)	636 @ 0.52 s	N/A	N/A	704 @ 0.54 s	922 @ 0.57 s

* Results are for partial loading only since simulations crash due to extreme temperatures at 0.70 ms (75 kJ) and 0.27 ms (150 kJ). The total energy loaded is thus 52.5 kJ and 40.5 kJ respectively.

and fits for the high temperature range (i.e. above the melting point [134]), beyond ~6000 K the fits must be extrapolated. All results at such high temperatures should be viewed with caution and serve the purpose only of being indicative of potentially dramatic levels of erosion by vaporization at the top surface (owing to the exponential scaling, the vaporization rate is 0.5 mm/ms at 8000 K and 22 mm/ms at 11000 K). Temperatures of this magnitude reached within the bulk could lead to explosion of material [127]. In fact, for $E_{RE} \geq 75$ kJ these very extreme temperatures are reached rather promptly at and just under the surface in the cases with fast loading (1 ms), and the runs crash.

Note further that the GEANT4 simulations are based on the original (unaltered) geometry and provide the energy density to be loaded as function of space. This energy density is then translated to a power density under the assumption of uniformity in time and is passed to MEMENTO. However, since the upper few tens of microns are promptly eroded, loading the GEANT4 map without any translation to compensate for the vaporization would lead to loss of energy deposited at the vaporized cells. The power density map is thus shifted along the radial direction to account for the fact that the free-surface position is moving in time.

The non-monotonic profiles near the top surface in Fig. 17a are a consequence of the exponential scaling of the vaporization flux: a very small increase in T_{surf} produces a substantial rise of the vaporization cooling flux so that cells on the free surface effectively receive less energy than those just below. Regarding the coolant interface temperature, comparing loading the same 50 kJ over 1 ms or 100 ms, the rapid deposition leads to much stronger vaporization due to the higher power densities, so that ~20 % of the incoming energy is lost due to vaporization cooling, versus only 0.01 % for the longer duration. Over the longer timescale loading, the active cooling contributes to reducing the interface temperature rise and both cases give roughly similar interface temperatures (Fig. 17b). For 100 ms loading at 50 and 200 kJ, in the latter case 34 % of the incoming energy is dissipated by vaporization loss due to the higher peak surface temperature so that, whilst the interface temperature is higher than for the 50 kJ load, it is lower than would be expected given the relative magnitudes (factor 4) in the energy deposition.

On the basis of these initial results, the peak cooling interface temperature (< 1000 K) is not a concern (note that a W/Cu bond is much more resilient than that of Be/Cu and will tolerate higher temperature excursions, though the actual threshold under the high pressure coolant conditions is not known quantitatively). It is, however, important to point out that the deposited energies simulated so far are still rather low in comparison to what could be experienced on ITER. An energy of 200 kJ deposited on a single apex corresponds to a RE current of only I_{RE} ~100 kA. If 200 kJ were to be deposited on each of the 36 apexes of the toroidal row of FW panels #8, the total of 7.2 MJ corresponds to I_{RE} ~3.6 MA and is thus equivalent to I_p ~5 MA assuming a maximum I_{RE} ~2/3 I_p (assuming no conversion of magnetic energy).

Further simulations with the higher fidelity workflow will explore higher E_{RE} and varying W thickness, but it is clear that beyond a given deposited energy, the simulations will fail once extreme values of T_{surf} are attained, even for the longer deposition times. Moreover, increased energy deposition will lead to higher melt depths, so that erosion due to single events can be severe, especially bearing in mind that a deep melt may not remain in place in the presence of strong thermionic emission currents and surface tension forces. At present, unlike the case of W melting due to thermal plasma impact, for which melt dynamics is now well understood [112], the stability and behaviour of RE induced W melts is still unknown. It is also clear that the highly idealised picture, modelled here, of a GEANT4 load map which remains constant through the transient, even in the presence of phase transitions and topological changes in the material, cannot be a true description of reality. Furthermore, intense vaporization into the RE plasma may drive some degree of vapour shielding and will impact the RE beam itself. None of this can be modelled at present and further physics development is required.

The situation is thus that if the RE transient is very rapid (~ms timescale) and sufficiently energetic, vaporization will be so intense that

erosion could be extremely dramatic in the absence of any vapour shield assist, or other mitigating impact on the RE beam. The number of events of this nature which could be tolerated is low, but can be increased by making the material thicker. They do not directly threaten the cooling interface, since an appreciable proportion of the incoming energy is dissipated through vaporization cooling and the only issue is whether or not repeated events can locally erode sufficient material to increase proximity to the interface. Whether or not such events could lead to mechanical damage (for example cracking or delamination of the W armour) is not known and is difficult to assess. It could conceivably be addressed by dedicated RE deposition experiments on current devices using actively cooled PFCs.

If the deposition time is longer (giving time for magnetic energy to be converted into RE energy), then melt depths can be significant even if surface temperatures are insufficient for strong vaporization. These longer deposition times are of course more penalising for the interface temperature unless the deposited energy is so high that vaporization once again dominates. There is, therefore, a strong argument for the W armour to be thickened in regions of the FW expected to be most susceptible to RE impact (e.g. the top of main chamber – see Fig. 16 – which also happens to be the region in which the unmitigated CQ thermal loads will be experienced (Section 6.1)) in order to improve resilience in the case of repeated events. This argument applies to both the provisional inertially cooled wall for SRO (when REs will be experienced for the first time on ITER) and for the final, actively cooled DT-1 wall, where, although runaway mitigation/avoidance will have been fully explored in the SRO campaigns, new RE seeds (due to Compton scattering of gamma rays from activated wall material and from tritium beta decay [105]) will be experienced for the first time. At the time of writing, the option of thickening the W armour option in critical locations on the poloidal contour is being adopted as part of the design activities for the new DT-1 full W wall.

Meanwhile, the higher fidelity RE deposition workflow is being directed to new code runs with much more sophisticated RE impact parameters. Instead of the idealised single grazing angle incidence at zero pitch angle and wetted area derived from DINA magnetic equilibria, more realistic RE footprints will be used from JOREK code studies of ITER RE termination [135]. In this work, a 3D fluid model for the RE's is implicitly coupled to the MHD equations, allowing the interaction of the RE current with MHD modes as well as VDEs to be calculated. Runaway beams of 9 MA are generated via the avalanche mechanism and are then lost rapidly (on timescales of ~1 ms), when stochastization of field lines occurs at the approach to $q_{95} = 2$ in the time-dependent 3D simulations. This leads to much more distributed RE impact. To calculate the FW RE energy loads on the FW, these MHD-RE fluid simulations are post-processed: RE particles are initialised right before the termination event according to the RE fluid density and two different analytic distributions for the momentum space. The full orbits of these particles are then traced in the time-evolving magnetic field until they collide with the 3D FW surface. The full pitch angle distribution (position and momentum vectors) and magnetic field components at every point on the FW panel surface can thus be provided to the GEANT4-MEMENTO workflow. In addition, the greater wetted surface reduces the energy density, though the energy maps and thermal transfer simulations are significantly more challenging computationally.

7. Conclusions

In response to technical delays and in order to provide a more rationalized approach to the nuclear safety demonstration, the ITER Organization decided in 2023 to begin a significant re-baselining exercise. One of the core elements of the new strategy is the switch from beryllium to tungsten amour on main chamber plasma-facing components. Although this does accelerate the deployment of a reactor relevant first wall material in ITER, brings the benefit of much higher resilience to transient heat loads, much reduced erosion and far lower fuel retention in comparison with beryllium, the increase by a factor ~5 in total area of tungsten facing the plasma is not without risk to plasma operation. This concerns primarily the increased core radiation levels resulting from higher tungsten contamination which may challenge both the achievement of the principal $Q = 10$ ITER DT burning plasma target, and reliable early current ramp-up in limiter configuration on tungsten surfaces.

Concerning burning plasmas, conservative assessments of the tungsten wall source obtained with erosion-migration simulations, together with integrated modelling of tungsten pedestal and core transport using codes benchmarked on experimental observations from smaller devices, demonstrate that the switch to tungsten on the first wall should present only a comparatively low risk to the $Q = 10$ goal. To mitigate this risk, the new re-baseline includes an increase in the planned electron cyclotron heating power.

Regarding limiter start-up, the unique new plasma boundary and integrated modelling analysis presented here, consistent with results from dedicated experiments on the EAST tokamak, likewise indicates that a tungsten wall should not present a major obstacle under the current ITER ramp-up scenario designs, provided central EC heating is available and low/medium Z impurity concentrations are not too high in the early stages. In today's devices, residual oxygen is often found to be problematic in this sense and its impact is typically reduced using different varieties of boronization wall conditioning. Based on this rich body of experience in the fusion community, ITER will install a diborane boronization system as part of the re-baseline. First-of-a-kind modelling studies of the boronization glow discharge performed at the ITER Organization have been instrumental in providing the physics specification for this system.

Given that fuel retention in an all-tungsten environment is rather low and essentially driven only by implantation, it is retention by co-deposition with boron eroded from coatings put down during the boronization process which will dominate if it turns out that procedure is routinely required during operation. Erosion-migration simulations taking into the 3D main chamber wall geometry demonstrate that the coating lifetime should be sufficient to provide adequate oxygen gettering capability through the planned standard 2-week operation cycle between short term maintenance periods, during which boronization could be performed if necessary. Even if such a coating frequency would be required in reality, the use of appropriate fuel recovery strategies during plasma operation (such as isotope exchange with ion cyclotron wall conditioning and the deployment of specific tokamak plasma configurations), together with thermal outgassing at the ends of main experimental campaigns, should be capable of maintaining much lower overall retention during nuclear operation than would have been the case with beryllium first wall armour, which represents an effectively infinite source of eroded material.

Unmitigated disruption thermal transients at high current/performance have always been an issue for the actively cooled ITER plasma-facing components, for which the original design basis was driven principally by the need to handle stationary loads. Events at the highest stored thermal and magnetic energies, particularly the disruption thermal and current quenches and runaway electron impact, would cause potentially severe melt damage on beryllium first wall surfaces. The much higher melting point of tungsten significantly increases the plasma current threshold at which FW melting will occur under current quench thermal loads. At the highest currents (and thus highest magnetic stored energies), 2D TOKES simulations demonstrate that tungsten vaporization should strongly reduce the incoming heat loads both by local plasma shielding and through tungsten radiation throughout the halo region. However, the shielding effect is much less effective at the threshold energy for melting, so that the impact in terms of material damage of current quench transients may actually be higher near the threshold current for melt onset than under the worst case events.

Unmitigated runaway electrons, with their potential to deposit energy deeper in the material bulk than experienced under typical

transient thermal plasma loads, are a threat on ITER whatever main chamber armour material is chosen. A simulation workflow permitting estimates of the likely melt damage and potential impact on bonding interfaces for actively cooled components has been developed at the ITER Organization and benchmarked with reasonable qualitative success against main chamber beryllium melt damage due to runaways formed by deliberate impurity injection on JET. With the switch to tungsten in the re-baseline, this workflow has been further improved by external collaborators and used to assess the consequences for runaway energy deposition on tungsten under simplified, but conservative loading conditions based on the dynamics observed at JET, including the planned actively cooled first wall geometry. The result is a recommendation for thickening of the tungsten armour compared to the previous beryllium first wall design in areas expected to be most susceptible to runaway impact. This should provide some tolerance in terms of material damage against a few unmitigated events in the early phase of DT operation when runaway seeds not previously experienced in early non-active operation will appear for the first time. This recommendation is now being adopted as a key input specification for the re-baselined first wall design. Even if such design decisions need to be made soon to satisfy the re-baseline schedule and as such must be based on the modelling workflow, it is clear that the potential for serious runaway electron damage and the complexity of the workflow provides strong motivation for future dedicated, well-diagnosed, controlled runaway electron impact experiments on current tokamaks, if possible using actively cooled components to characterize both erosion depth and possible mechanical damage to the armour/substrate bond interface.

All of these plasma-wall interaction issues figure prominently in the rationale for the revised re-baseline ITER Research Plan. Importantly, the two original non-active Pre-Fusion Power Operation (PFPO) phases are now replaced by a single Start of Research Operation (SRO) campaign which is to be executed with a provisional, non-actively cooled tungsten first wall, for which, at the time of publication of this article, the conceptual design review has just been presented. This will permit the development of routine plasma start-up on tungsten surfaces and includes, as a key SRO deliverable, the achievement of hydrogen L-mode operation at the nominal machine current and field (15 MA / 5.3 T).

In contrast to the 2016 Baseline PFPO campaigns, SRO also comprises a short (~2 month) deuterium plasma phase, marking the formal start of ITER nuclear operation, and hopefully allowing a first look at (ELMing) H-modes at half toroidal field and lower current. In addition, it presents the opportunity to gain experience of H-D-H isotope exchange, including the use of ion cyclotron wall conditioning, and to put the planned fuel recovery strategies to the test. Boronization wall conditioning will be possible from the start of SRO, which thus becomes an important calibration phase to determine first if it is necessary at all for routine operation and, if it is, to assess its impact on the key issues of fuel retention/recovery and dust formation due to the predicted migration of eroded boron to remote areas.

The biggest drivers for beginning operation with an inertially cooled wall are disruption transients. Although the new Research Plan is to a large extent constructed around the validation of unmitigated disruption thermal and electromagnetic loads and the commissioning and full deployment of the Disruption Mitigation System (DMS), it is in the SRO phase that disruptivity will be highest. Moreover, the DMS action in itself is expected to be the most significant cause of runaway electron generation, even if the system is designed specifically to prevent both natural and self-generated events. Nevertheless, single events, even at comparatively low runaway current, can in principle pose a threat to cooling channel integrity. By beginning operation with temporary first wall, the revised Research Plan crucially provides a more sensible option in which disruption avoidance and mitigation in a device capable of unprecedented thermal and runaway loads can be developed without fear of compromising the integrity of extremely complex, costly and difficult to replace actively cooled first wall plasma-facing components. It also permits the development of robust avoidance and mitigation schemes before the installation of the final actively cooled wall prior to the DT operation phase.

CRediT authorship contribution statement

R.A. Pitts: Writing – review & editing, Writing – original draft, Supervision, Project administration, Investigation, Formal analysis, Conceptualization. **A. Loarte:** Investigation, Formal analysis, Conceptualization. **T. Wauters:** Investigation, Formal analysis, Conceptualization. **M. Dubrov:** Visualization, Software, Formal analysis. **Y. Gribov:** Formal analysis. **F. Köchl:** Software, Formal analysis. **A. Pshenov:** Software, Formal analysis. **Y. Zhang:** Software, Formal analysis. **J. Artola:** Formal analysis. **X. Bonnin:** Software, Formal analysis. **L. Chen:** Formal analysis. **M. Lehnen:** Conceptualization. **K. Schmid:** Software, Formal analysis. **R. Ding:** Investigation. **H. Frerichs:** Formal analysis. **R. Futtersack:** Software. **X. Gong:** Supervision. **G. Hagelaar:** Investigation, Formal analysis. **E. Hodille:** Software, Formal analysis. **J. Hobirk:** Methodology, Investigation. **S. Krat:** Investigation, Formal analysis. **D. Matveev:** Software, Formal analysis. **K. Paschalidis:** Software, Formal analysis. **J. Qian:** Methodology, Investigation. **S. Ratynskaia:** Supervision, Formal analysis. **T. Rizzi:** Software, Formal analysis. **V. Rozhansky:** Investigation. **P. Tamain:** Supervision, Investigation. **P. Tolias:** Supervision, Formal analysis. **L. Zhang:** Software, Formal analysis. **W. Zhang:** Software, Formal analysis.

Declaration of competing interest

The authors declare that they have no known competing financial interests or personal relationships that could have appeared to influence the work reported in this paper.

Acknowledgements

The views and opinions expressed herein do not necessarily reflect those of the ITER Organization. ITER is the nuclear facility INB 174. Several of the co-authors have contributed within the framework of the ITER Scientist Fellowship Network (ISFN).

Data availability

Data will be made available on request.

References

[1] R.A. Pitts, Y. Gribov, J. Coburn, F. Fuentes, et al., First wall power flux management during plasma current ramp-up on ITER, Nucl. Fusion 62 (2022), https://doi.org/10.1088/1741-4326/ac8062.
[2] A. Kallenbach, R. Dux, M. Mayer, R. Neu, et al., Non-boronized compared with boronized operation of ASDEX pgrade with full-tungsten plasma ufacing components, Nucl. Fusion 49 (2009), https://doi.org/10.1088/0029-5515/49/4/045007.
[3] J. Bucalossi, J. Achard, O. Agullo, T. Alarcon, et al., Operating a full tungsten actively cooled tokamak: overview of WEST first phase of operation, Nucl. Fusion 62 (2022), https://doi.org/10.1088/1741-4326/ac2525.
[4] X. Gong, Y. Song, B. Wan, J. Li, et al., Overview of recent experimental results on the EAST Tokamak, Nucl. Fusion 64 (2024), https://doi.org/10.1088/1741-4326/ad4270.
[5] M. Greenwald, A. Bader, S. Baek, M. Bakhtiari, et al., 20 years of research on the Alcator C-Mod tokamak, Phys. Plasmas 21 (2014), https://doi.org/10.1063/1.4901920.
[6] W.H. Ko, S.W. Yoon, W.C. Kim, J.G. Kwak, et al., Overview of the KSTAR experiments toward fusion reactor, Nucl. Fusion 64 (2024), https://doi.org/10.1088/1741-4326/ad3b1d.
[7] P. Vondracek, R. Panek, M. Hron, J. Havlicek, et al., Preliminary design of the COMPASS upgrade tokamak, Fusion Eng. Des. 169 (2021), https://doi.org/10.1016/j.fusengdes.2021.112490.
[8] F. Crisanti, R. Ambrosino, M.V. Falessi, L. Gabellieri, et al., Physics basis for the divertor tokamak test facility, Nucl. Fusion 64 (2024), https://doi.org/10.1088/1741-4326/ad6e06.

[9] A.J. Creely, M.J. Greenwald, S.B. Ballinger, D. Brunner, et al., Overview of the SPARC tokamak, J. Plasma Phys. 86 (2020), https://doi.org/10.1017/S0022377820001257.

[10] A. Loarte, R. A. Pitts, T. Wauters, I. Nunes et al., Initial evaluations in support of the new ITER baseline and Research Plan, ITER Technical Report ITR-24-004 (2024). https://www.iter.org/scientists/iter-technical-reports.

[11] A. Loarte et al., The new ITER Baseline, Research Plan and open R&D issues, submitted to Plasma Phys. Control. Fusion.

[12] D.J. Campbell, A. Loarte, D. Boilson, X. Bonnin, et al., ITER research plan within the staged approach (Level III-Final Version), ITER Tech. Rep. ITR-24-005 (2024). https://www.iter.org/scientists/iter-technical-reports.

[13] R.A. Pitts, X. Bonnin, F. Escourbiac, H. Frerichs, et al., Physics basis for the first ITER tungsten divertor, Nucl. Mater. Energy 20 (2019), https://doi.org/10.1016/j.nme.2019.100696.

[14] E. Joffrin, M. Baruzzo, M. Beurskens, C. Bourdelle, et al., First scenario development with the JET new ITER-like wall, Nucl. Fusion 54 (2014), https://doi.org/10.1088/0029-5515/54/1/013011.

[15] J. Schweinzer, M. Beurskens, L. Frassinetti, E. Joffrin, et al., Development of the Q = 10 scenario for ITER on ASDEX Upgrade (AUG), Nucl. Fusion 56 (2016), https://doi.org/10.1088/0029-5515/56/10/106007.

[16] C. Angioni, M. Sertoli, R. Bilato, V. Bobkov, et al., A comparison of the impact of central ECRH and central ICRH on the tungsten behaviour in ASDEX Upgrade H-mode plasmas, Nucl. Fusion 57 (2017), https://doi.org/10.1088/1741-4326/aa6453.

[17] A. Loarte, M.L. Reinke, A.R. Polevoi, M. Hosokawa, et al., Tungsten impurity transport experiments in Alcator C-Mod to address high priority research and development for ITER, Phys. Plasmas 22 (2015), https://doi.org/10.1063/1.4921253.

[18] R. Dux, A. Loarte, C. Angioni, D. Coster, et al., The interplay of controlling the power exhaust and the tungsten content in ITER, Nucl. Mater. Energy 12 (2017) 28–35, https://doi.org/10.1016/j.nme.2016.10.013.

[19] R. Dux, V. Bobkov, A. Herrmann, A. Janzer, et al., Plasma-wall interaction and plasma behaviour in the non-boronised all tungsten ASDEX upgrade, J. Nucl. Mater. 390–391 (2009) 858–863, https://doi.org/10.1016/j.jnucmat.2009.01.225.

[20] R. Dux, A. Janzer, T. Pütterich, Erratum: Main chamber sources and edge transport of tungsten in H-mode plasmas at ASDEX Upgrade, Nucl. Fusion 51 (2011), https://doi.org/10.1088/0029-5515/51/11/119501.

[21] D. Fajardo, C. Angioni, P. Maget, P. Manas, Analytical model for collisional impurity transport in tokamaks at arbitrary collisionality, Plasma Phys Control Fusion 64 (2022), https://doi.org/10.1088/1361-6587/ac5b4d.

[22] R. Dux, A. Loarte, E. Fable, A. Kukushkin, Transport of tungsten in the H-mode edge transport barrier of ITER, Plasma Phys. Control. Fusion 56 (2014), https://doi.org/10.1088/0741-3335/56/12/124003.

[23] D.C. Van Vugt, G.T.A. Huijsmans, M. Hoelzl, A. Loarte, Kinetic modeling of ELM-induced tungsten transport in a tokamak plasma, Phys. Plasmas 26 (2019), https://doi.org/10.1063/1.5092319.

[24] A. Loarte, G. Huijsmans, S. Futatani, L.R. Baylor, et al., Progress on the application of ELM control schemes to ITER scenarios from the non-active phase to DT operation, Nucl. Fusion 54 (2014), https://doi.org/10.1088/0029-5515/54/3/033007.

[25] S.Q. Korving, V. Mitterauer, G.T.A. Huijsmans, A. Loarte, et al., Simulation of neoclassical heavy impurity transport in ASDEX Upgrade with applied 3D magnetic fields using the nonlinear MHD code JOREK, Phys. Plasmas 31 (2024), https://doi.org/10.1063/5.0198299.

[26] M. Romanelli, G. Corrigan, V. Parail, S. Wiesen, et al., JINTRAC: a system of codes for integrated simulation of Tokamak scenarios, Plasma Fusion Res. 9 (2014), https://doi.org/10.1585/pfr.9.3403023.

[27] E. Fransson, H. Nordman, P. Strand, Upgrade and benchmark of quasi-linear transport model EDWM, Phys. Plasmas 29 (2022), https://doi.org/10.1063/5.0119515.

[28] E.A. Belli, J. Candy, Full linearized Fokker-Planck collisions in neoclassical transport simulations, Plasma Phys. Control. Fusion 54 (2012), https://doi.org/10.1088/0741-3335/54/1/015015.

[29] K. Schmid, M. Reinelt, K. Krieger, An integrated model of impurity migration and wall composition dynamics for tokamaks, J. Nucl. Mater. 415 (2011), https://doi.org/10.1016/j.jnucmat.2011.01.105.

[30] K. Schmid, T. Wauters, Full W ITER: Assessment of expected W erosion and implications of boronization on fuel retention, Nucl. Mater. Energy 41 (2024), https://doi.org/10.1016/j.nme.2024.101789.

[31] H.D. Pacher, A.S. Kukushkin, G.W. Pacher, V. Kotov, et al., Impurity seeding in ITER DT plasmas in a carbon-free environment, J. Nucl. Mater. 463 (2015) 591–595, https://doi.org/10.1016/j.jnucmat.2014.11.104.

[32] J. Romazanov, A. Kirschner, S. Brezinsek, R.A. Pitts, et al., Beryllium erosion and redeposition in ITER H, He and D-T discharges, Nucl. Fusion 62 (2022), https://doi.org/10.1088/1741-4326/ac4776.

[33] N. Vianello, D. Carralero, C.K. Tsui, V. Naulin, et al., Scrape-off layer transport and filament characteristics in high-density tokamak regimes, Nucl. Fusion 66 (2020), https://doi.org/10.1088/1741-4326/ab423e.

[34] K. Schmid, K. Krieger, S.W. Lisgo, G. Meisl, et al., WALLDYN simulations of global impurity migration in JET and extrapolations to ITER, Nucl. Fusion 55 (2015), https://doi.org/10.1088/0029-5515/55/5/053015.

[35] A. Khan, G. De Temmerman, S.W. Lisgo, X. Bonnin, et al., WallDYN simulations of material migration and fuel retention in ITER low power H plasmas and high power neon-seeded DT plasmas, Nucl. Mater. Energy 20 (2019), https://doi.org/10.1016/j.nme.2019.100674.

[36] S. Rode, S. Brezinsek, M. Groth, A. Kirschner, et al., Multi-staged ERO2.0 simulation of material erosion and deposition in recessed mirror assemblies in JET and ITER, Nucl. Fusion 64 (2024), https://doi.org/10.1088/1741-4326/ad556d.

[37] D. Reiter, M. Baelmans, P. Börner, The EIRENE and B2-EIRENE codes, Fusion Sci. Technol. 47 (2005), https://doi.org/10.13182/FST47-172.

[38] X. Bonnin, W. Dekeyser, R.A. Pitts, D. Coster, et al., Presentation of the new SOLPS-ITER code package for tokamak plasma edge modelling, Plasma Fusion Res. 11 (2016), https://doi.org/10.1585/pfr.11.1403102.

[39] S. Wiesen, D. Reiter, V. Kotov, M. Baelmans, et al., The new SOLPS-ITER code package, J. Nucl. Mater. 463 (2015), https://doi.org/10.1016/j.jnucmat.2014.10.012.

[40] W. Dekeyser, P. Boerner, S. Voskoboynikov, V.A. Rozhanksy, et al., Plasma edge simulations including realistic wall geometry with SOLPS-ITER, Nucl. Mater. Energy 27 (2021), https://doi.org/10.1016/j.nme.2021.100999.

[41] H. Bufferand, P. Tamain, S. Baschetti, J. Bucalossi, et al., Three-dimensional modelling of edge multi-component plasma taking into account realistic wall geometry, Nucl. Mater. Energy 18 (2019), https://doi.org/10.1016/j.nme.2018.11.025.

[42] N. Rivals, P. Tamain, Y. Marandet, X. Bonnin, et al., Impact of enhanced far-SOL transport on first wall fluxes in ITER from full vessel edge-plasma simulations, Nucl. Mater. Energy 33 (2022), https://doi.org/10.1016/j.nme.2022.101293.

[43] S. Sureshkumar, N. Rivals, P. Tamain, X. Bonnin, et al., First SOLEDGE3X-EIRENE simulations of the ITER Neon seeded burning plasma boundary up to the first wall, Nucl. Mater. Energy 41 (2024), https://doi.org/10.1016/j.nme.2024.101780.

[44] W. Zhang, A. Messiaen, W. Helou, V. Bobkov, et al., Parametric study of midplane gas puffing to maximize ICRF power coupling in ITER, Nucl. Fusion 63 (2023), https://doi.org/10.1088/1741-4326/acb4ad.

[45] G.F. Matthews, Plasma operation with an all metal first-wall: comparison of an ITER-like wall with a carbon wall in JET, J. Nucl. Mater. 438 (2013), https://doi.org/10.1016/j.jnucmat.2013.01.282.

[46] J. Winter, H.G. Esser, L. Kiinen, V. Philipps, et al., Boronization in TEXTOR, J. Nucl. Mater. 162–164 (1989) 713.

[47] M. Dibon, V. Rohde, F. Stelzer, K. Hegele, et al., New boronization system at ASDEX Upgrade, Fusion Eng. Des. 165 (2021), https://doi.org/10.1016/j.fusengdes.2021.112233.

[48] G. Jackson, J. Winter, K. Burrell, J. DeBoo, et al., Boronization in DIII-D, J. Nucl. Mater. 196–198 (1992) 236.

[49] H.G. Esser, S.J. Fielding, S.D. Hanks, P.C. Johnson, et al., Boronization of COMPASS, J. Nucl. Mater. 186 (1992) 217.

[50] C. Boucher, F. Martin, B.L. Stansfield, B. Terreault, et al., Comparison of three boronization techniques in TdeV, J. Nucl. Mater. 196–198 (1992) 587.

[51] R. Ochoukov, D. Whyte, B. Lipschultz, B. Labombard, et al., Study and optimization of boronization in Alcator C-Mod using the Surface Science Station (S^3), Fusion Eng. Des. 87 (2012) 1700, https://doi.org/10.1016/j.fusengdes.2012.07.013.

[52] T. Wauters, G.J.M. Hagelaar, R.A. Pitts, Modeling input to the ITER glow discharge boronization system design, this conference paper P4-059. Accepted in Nuclear Materials and Energy.

[53] G.J.M. Hagelaar, D. Kogut, D. Douai, R.A. Pitts, Modelling of tokamak glow discharge cleaning I: physical principles, Plasma Phys. Control. Fusion 57 (2015), https://doi.org/10.1088/0741-3335/57/2/025008.

[54] M.M. Ennaceur, B. Terreault, XPS study of the process of oxygen gettering by thin films of PACVD boron, J. Nucl. Mater. 280 (2000) 33.

[55] K. Schmid, T. Lunt, 3D global impurity transport modeling with WallDYN and EMC3-Eirene, Nucl. Mater. Energy 17 (2018), https://doi.org/10.1016/j.nme.2018.11.005.

[56] R. A. Pitts, G. De Temmerman et al., Progress in the understanding of Plasma-Wall Interactions in support of the ITER Research Plan, 47th EPS Conference on Plasma Physics, 21-25 June 2021 (virtual) I1.001.

[57] N. Taylor, S. Ciattaglia, P. Cortes, M. Iseli, et al., ITER safety and licensing update, Fusion Eng. Des. 87 (2012), https://doi.org/10.1016/j.fusengdes.2012.01.001.

[58] P. Shigin, N. Babinov, G. De Temmerman, A. Danisi, et al., RF discharge mirror cleaning system development for ITER diagnostics, Fusion Eng. Des. 164 (2021), https://doi.org/10.1016/j.fusengdes.2020.112162.

[59] G. De Temmerman, M.J. Baldwin, R.P. Doerner, D. Nishijima, et al., An empirical scaling for deuterium retention in co-deposited beryllium layers, Nucl. Fusion 48 (2008), https://doi.org/10.1088/0029-5515/48/7/075008.

[60] A. Zaloznik, M.J. Baldwin, R.P. Doerner, G. De Temmerman, et al., Improved scaling law for the prediction of deuterium retention in beryllium co-deposits, Nucl. Fusion 62 (2022), https://doi.org/10.1088/1741-4326/ac4775.

[61] C.C. Tsai, Characterization of amorphous semiconducting silicon-boron alloys prepared by plasma decomposition, Phys. Rev. B 19 (1979) 2041.

[62] H. Toyoda, Control of hydrogen content of boron thin films produced in a dc toroidal discharge, Appl. Phys. Lett. 51 (1987) 798.

[63] M. Yamage, T. Ejima, M. Saidoh, N. Ogiwara, H. Sugai, Wall temperature dependence of boronization using decaborane and diborane, Jpn. J. Appl. Phys. 32 (1993) 3968.

[64] Y. Ito, et al., Electron cyclotron resonance discharge of sublimation gas of decaborane and its application to preparation of boron thin films, Jpn. J. Appl. Phys. 33 (1994) 4251.

[65] A. Annen, M. Sag, R. Beckmann, W. Jacob, Stability of plasma-deposited amorphous hydrogenated boron films, Thin Solid Films 300 (1997) 101.

[66] J. Roth, E. Tsitrone, A. Loarte, T. Loarer, et al., Recent analysis of key plasma wall interactions issues for ITER, J. Nucl. Mater. 390–391 (2009), https://doi.org/10.1016/j.jnucmat.2009.01.037.

[67] G. De Temmerman, R.P. Doerner, Deuterium retention and release in tungsten co-deposited layers, J. Nucl. Mater. 389 (2009), https://doi.org/10.1016/j.jnucmat.2009.03.028.

[68] V.K. Alimov, J. Roth, W.M. Shu, D.A. Komarov, et al., Deuterium trapping in tungsten deposition layers formed by deuterium plasma sputtering, J. Nucl. Mater. 399 (2010), https://doi.org/10.1016/j.jnucmat.2010.01.024.

[69] S. Krat, et al., Tungsten-deuterium co-deposition: experiment and analytical description, Vacuum 149 (2017) 23.

[70] R. Causey, D. Walsh, Co-deposition of deuterium with beryllium, J. Nucl. Mater. 254 (1998) 84.

[71] M.J. Baldwin, M.J. Simmonds, G. De Temmerman, R.P. Doerner, Deuterium retention in Be-D co-deposits formed over an ITER relevant parameter space, Phys. Scr. T171 (2020), https://doi.org/10.1088/1402-4896/ab41a3.

[72] W.R. Wampler, B. Labombard, B. Lipschultz, G.M. Mccracken, et al., Molybdenum erosion measurements in Alcator C-Mod, J. Nucl. Mater. 266–269 (1999) 217.

[73] K. Krieger, M. Balden, A. Bortolon, R. Dux, et al., Wall conditioning effects and boron migration during boron powder injection in ASDEX upgrade, Nucl. Mater. Energy 34 (2023), https://doi.org/10.1016/j.nme.2023.101374.

[74] R. Delaporte-Mathurin, H. Yang, J. Denis, J. Dark, et al., Fuel retention in WEST and ITER divertors based on FESTIM monoblock simulations, Nucl. Fusion 61 (2021), https://doi.org/10.1088/1741-4326/ac2bbd.

[75] T. Wauters, D. Matveev, D. Douai, J. Banks, et al., Isotope removal experiment in JET-ILW in view of T-removal after the 2nd DT campaign at JET, Phys. Scr. 97 (2022), https://doi.org/10.1088/1402-4896/ac5856.

[76] D. Matveev, D. Douai, T. Wauters, A. Widdowson, et al., Tritium removal from JET-ILW after T and D-T experimental campaigns, Nucl. Fusion 63 (2023), https://doi.org/10.1088/1741-4326/acf0d4.

[77] J.S. Park, X. Bonnin, R.A. Pitts, Y. Gribov, et al., Feasibility of raised inner strike point equilibria scenario in ITER for detritiation from beryllium co-deposits, Nucl. Fusion 63 (2023), https://doi.org/10.1088/1741-4326/acd9d9.

[78] S. Brezinsek, T. Loarer, V. Philipps, H.G. Esser, et al., Fuel retention studies with the ITER-Like Wall in JET, Nucl. Fusion 53 (2013), https://doi.org/10.1088/0029-5515/53/8/083023.

[79] A. Widdowson, J.P. Coad, Y. Zayachuk, I. Jepu, et al., Evaluation of tritium retention in plasma facing components during JET tritium operations, Phys. Scr. 96 (2021), https://doi.org/10.1088/1402-4896/ac3b30.

[80] J. Romazanov, S. Brezinsek, C. Baumann, S. Rode, et al., Validation of the ERO2.0 code using W7-X and JET experiments and predictions for ITER operation, Nucl. Fusion 64 (2024), https://doi.org/10.1088/1741-4326/ad5368.

[81] G. De Temmerman, M.J. Baldwin, D. Anthoine, K. Heinola, et al., Efficiency of thermal outgassing for tritium retention measurement and removal in ITER, Nucl. Mater. Energy 12 (2017), https://doi.org/10.1016/j.nme.2016.10.016.

[82] D. Matveev, M. Zlobinski, G. De Temmerman, B. Unterberg, et al., CRDS modelling of deuterium release from co-deposited beryllium layers in temperature programmed and laser induced desorption experiments, Phys. Scr. T171 (2020), https://doi.org/10.1088/1402-4896/ab5569.

[83] E.A. Hodille, X. Bonnin, R. Bisson, T. Angot, et al., Macroscopic rate equation modeling of trapping/detrapping of hydrogen isotopes in tungsten materials, J. Nucl. Mater. 467 (2015), https://doi.org/10.1016/j.jnucmat.2015.06.041.

[84] A. Annen, R. Beckmann, W. Jacob, Deposition and characterization of dense and stable amorphous hydrogenated boron films at low substrate temperatures, J. Non Cryst. Solids 209 (1997) 240.

[85] T. Nakahata, A. Yoshikawa, M. Oyaidzu, Y. Oya, et al., Dynamics of deuterium implanted in boron coating film for wall conditioning, J. Nucl. Mater. 367–370 (2007) 1170, https://doi.org/10.1016/j.jnucmat.2007.03.209.

[86] Y. Oya, H. Kodama, M. Oyaidzu, Y. Morimoto, et al., Implanted hydrogen isotope retention and chemical behavior in boron thin films for wall conditioning, J. Nucl. Mater. 329–333 (2004), https://doi.org/10.1016/j.jnucmat.2004.04.279.

[87] O. Gruber, A.C.C. Sips, R. Dux, T. Eich, et al., Compatibility of ITER scenarios with full tungsten wall in ASDEX upgrade, Nucl. Fusion 49 (2009), https://doi.org/10.1088/0029-5515/49/11/115014.

[88] R. Neu, V. Bobkov, R. Dux, J.C. Fuchs, et al., Ten years of W programme in ASDEX upgrade - challenges and conclusions, Phys. Scr. T138 (2009), https://doi.org/10.1088/0031-8949/2009/T138/014038.

[89] I. Zammuto, L. Giannone, A. Herrmann, A. Houben, et al., Implementation of ferritic steel as in vessel wall: Lessons learnt and follow up, Fusion Eng. Des. 124 (2017), https://doi.org/10.1016/j.fusengdes.2017.04.016.

[90] P. Maget, P. Manas, J.F. Artaud, C. Bourdelle, et al., Healing plasma current ramp-up by nitrogen seeding in the full tungsten environment of WEST, Plasma Phys. Control. Fusion 64 (2022), https://doi.org/10.1088/1361-6587/ac4b93.

[91] R.R. Khayrutdinov, V.E. Lukash, Studies of plasma equilibrium and transport in a tokamak fusion device with the inverse-variable technique, J. Comput. Phys. 109 (1993) 193.

[92] R. Behrisch, W. Eckstein, Sputtering by Particle Bombardment, Springer, Berlin Heidelberg New York, 2007.

[93] M. Kocan, R.A. Pitts, G. Arnoux, I. Balboa, et al., Impact of a narrow limiter SOL heat flux channel on the ITER first wall panel shaping, Nucl. Fusion 55 (2015), https://doi.org/10.1088/0029-5515/55/3/033019.

[94] Y. Gribov et al., DINA simulations of ITER 15 MA hydrogen L-mode scenarios with tungsten first wall, in: 50th EPS Conference on Plasma Physics (2024) P4-090.

[95] M. Fichtmüller, Core-edge coupling and the effect of the EDGE on overall plasma performance, Czech J. Phys. 48 (1998) 25.

[96] H. P. Summers, N R Badnell1, M G O'Mullane1, A D Whiteford et al., Atomic data for modelling fusion and astrophysical plasmas, Plasma Phys. Control. Fusion **44** (2002) B323. stacks.iop.org/PPCF/44/B323.

[97] G.M. Staebler, J.E. Kinsey, R.E. Waltz, Gyro-Landau fluid equations for trapped and passing particles, Phys. Plasmas 12 (2005), https://doi.org/10.1063/1.2044587.

[98] S. Wiesen, S. Brezinsek, A. Järvinen, T. Eich, et al., Integrated modelling of a JET type-I ELMy H-mode pulse and predictions for ITER-like wall scenarios, Plasma Phys. Control. Fusion 53 (2011), https://doi.org/10.1088/0741-3335/53/12/124039.

[99] D. Farina, A quasi-optical beam-tracing code for electron cyclotron absorption and current drive: GRAY, Fusion Sci. Technol. 52 (2007) 154.

[100] T. Hirai, S. Carpentier-Chouchana, F. Escourbiac, S. Panayotis, et al., Design optimization of the ITER tungsten divertor vertical targets, Fusion Eng. Des. 127 (2018), https://doi.org/10.1016/j.fusengdes.2017.12.007.

[101] J. Li, M. Shimada, Y. Zhao, J. Hu, et al., Wall conditioning towards the utilization in ITER, J. Nucl. Mater. 415 (2011), https://doi.org/10.1016/j.jnucmat.2010.10.048.

[102] S. Fietz, E. Fable, J. Hobirk, R. Fischer, et al., Investigation of transport models in ASDEX Upgrade current ramps, Nucl. Fusion 53 (2013), https://doi.org/10.1088/0029-5515/53/5/053004.

[103] M. Henderson, G. Saibene, C. Darbos, D. Farina, et al., The targeted heating and current drive applications for the ITER electron cyclotron system, Phys. Plasmas 22 (2015), https://doi.org/10.1063/1.4908598.

[104] A. Geier, K. Krieger, R. Neu, D.P. Coster, et al., Modelling of tungsten migration during limiter ramp-down in the ASDEX Upgrade divertor tokamak, Nucl. Fusion 45 (2005), https://doi.org/10.1088/0029-5515/45/8/011.

[105] O. Vallhagen, L. Hanebring, F.J. Artola, M. Lehnen, et al., Runaway electron dynamics in ITER disruptions with shattered pellet injections, Nucl. Fusion 64 (2024), https://doi.org/10.1088/1741-4326/ad54d7.

[106] R. A. Pitts, S. Pestchanyi, M. Lehnen, G. Saibene, TOKES simulations of first wall and divertor damage during unmitigated disruptions on ITER, 29th Fusion Energy Conference (FEC 2023), 2023. IAEA-CN-316-2152.

[107] F.J. Artola, N. Schwarz, S. Gerasimov, A. Loarte, et al., Modelling of vertical displacement events in tokamaks: status and challenges ahead, Plasma Phys. Control. Fusion 66 (2024), https://doi.org/10.1088/1361-6587/ad38d7.

[108] L. Kos, R.A. Pitts, G. Simič, M. Brank, et al., SMITER: a field-line tracing environment for ITER, Fusion Eng. Des. 146 (2019), https://doi.org/10.1016/j.fusengdes.2019.03.037.

[109] E. Thorén, S. Ratynskaia, P. Tolias, R.A. Pitts, The MEMOS-U code description of macroscopic melt dynamics in fusion devices, Plasma Phys. Control. Fusion 63 (2021), https://doi.org/10.1088/1361-6587/abd838.

[110] J. Coburn, M. Lehnen, R.A. Pitts, G. Simic, et al., Energy deposition and melt deformation on the ITER first wall due to disruptions and vertical displacement events, Nucl. Fusion 62 (2022), https://doi.org/10.1088/1741-4326/ac38c7.

[111] I. Jepu, G.F. Matthews, A. Widdowson, M. Rubel, et al., Beryllium melting and erosion on the upper dump plates in JET during three ITER-like wall campaigns, Nucl. Fusion 59 (2019), https://doi.org/10.1088/1741-4326/ab2076.

[112] S. Ratynskaia, E. Thorén, P. Tolias, R.A. Pitts, et al., Resolidification-controlled melt dynamics under fast transient tokamak plasma loads, Nucl. Fusion 60 (2020), https://doi.org/10.1088/1741-4326/abadac.

[113] S. Ratynskaia, K. Paschalidis, K. Krieger, L. Vignitchouk, et al., Metallic melt transport across castellated tiles, Nucl. Fusion 64 (2024), https://doi.org/10.1088/1741-4326/ad219b.

[114] L. Vignitchouk, S. Ratynskaia, R. Pitts, M. Lehnen, Beryllium melt instabilities and ejection during unmitigated current quenches in ITER, Nucl. Fusion 63 (2023), https://doi.org/10.1088/1741-4326/aca167.

[115] K. Ibano, Y. Kikuchi, S. Togo, Y. Ueda, et al., Estimation of suppressed erosion by vapor shielding at Be and W walls under transient loads, Nucl. Fusion 59 (2019), https://doi.org/10.1088/1741-4326/ab0977.

[116] I.S. Landman, Tokamak Code TOKES: models and Implementation, Forschungszentrum Karlsruhe report FZKA-7496 (2009).

[117] S. Pestchanyi, R.A. Pitts, V. Safronov, Validation of TOKES vapor shield simulations against experiments in the 2MK-200 facility, Fusion Eng. Des. 124 (2017), https://doi.org/10.1016/j.fusengdes.2017.02.048.

[118] M. Lehnen, K. Aleynikova, P.B. Aleynikov, D.J. Campbell, et al., Disruptions in ITER and strategies for their control and mitigation, J. Nucl. Mater. 463 (2015), https://doi.org/10.1016/j.jnucmat.2014.10.075.

[119] K. Krieger et al., ITPA Special Issue "On the Path to Burning Plasma Operation", Chapter 5: Scrape-off layer and divertor physics, accepted for publication in Nuclear Fusion (2024).

[120] H.-W. Bartels, Impact of runaway electrons, Fusion Eng. Des. 23 (1993) 323.

[121] A. Cardella, H. Gorenflo, A. Lodato, K. Ioki, et al., Effects of plasma disruption events on ITER first wall materials, J. Nucl. Mater. 283–287 (2000) 1105.

[122] G. Maddaluno, G. Maruccia, M. Merola, S. Rollet, Energy deposition and thermal effects of runaway electrons in ITER-FEAT plasma facing components, J. Nucl. Mater. 313–316 (2003) 651.

[123] V. Sizyuk, A. Hassanein, Self-consistent analysis of the effect of runaway electrons on plasma facing components in ITER, Nucl. Fusion 49 (2009), https://doi.org/10.1088/0029-5515/49/9/095003.

[124] B. Bazylev, G. Arnoux, S. Brezinsek, Y. Igitkhanov, et al., Modeling of the impact of runaway electrons on the ILW in JET, J. Nucl. Mater. 438 (2013), https://doi.org/10.1016/j.jnucmat.2013.01.035.

[125] C. Reux, V. Plyusnin, B. Alper, D. Alves, et al., Runaway electron beam generation and mitigation during disruptions at JET-ILW, Nucl. Fusion 55 (2015), https://doi.org/10.1088/0029-5515/55/9/093013.
[126] M. Diez, Y. Corre, E. Delmas, N. Fedorczak, et al., In-situ observation of tungsten plasma-facing components after the first phase of operation of the WEST tokamak, Nucl. Fusion 61 (2021), https://doi.org/10.1088/1741-4326/ac1dc6.
[127] M. De Angeli, P. Tolias, S. Ratynskaia, D. Ripamonti, et al., Evidence for high-velocity solid dust generation induced by runaway electron impact in FTU, Nucl. Fusion 63 (2023), https://doi.org/10.1088/1741-4326/ac8a04.
[128] I. Jepu, A. Widdowson, G. Matthews, J.P. Coad, et al., Overview of damage to beryllium limiters by unmitigated disruptions and runaway electrons in the JET tokamak with metal walls, Nucl. Fusion 64 (2024), https://doi.org/10.1088/1741-4326/ad6614.
[129] J. Allison, K. Amako, J. Apostolakis, P. Arce et al., Recent developments in GEANT4, Nuclear Instruments and. Methods in Phys Res A **835** (2016). DOI: 10.1016/j.nima.2016.06.125.
[130] L. Chen, R. A. Pitts, M. Lehnen et al., Modeling runaway electron induced damage to ITER plasma-facing components, 5th Asia-Pacific Conference on Plasma Physics, 2021: MF2-II4.
[131] K. Paschalidis, F. Lucco Castello, S. Ratynskaia, P. Tolias et al., The MEMENTO code for modeling of macroscopic melt motion in fusion devices, Fusion Engineering and Design **206** (2024). DOI: 10.1016/j.fusengdes.2024.114603.
[132] K. Paschalidis, S. Ratynskaia, F. Lucco Castello, P. Tolias, Melt dynamics with MEMENTO — code development and numerical benchmarks, Nucl. Mater. Energy 37 (2023), https://doi.org/10.1016/j.nme.2023.101545.
[133] A.R. Raffray, B. Calcagno, P. Chappuis, Z. Fu, et al., The ITER blanket system design challenge, Nucl. Fusion 54 (2014), https://doi.org/10.1088/0029-5515/54/3/033004.
[134] P. Tolias, Analytical expressions for thermophysical properties of solid and liquid tungsten relevant for fusion applications, Nucl. Mater. Energy 13 (2017), https://doi.org/10.1016/j.nme.2017.08.002.
[135] H. Bergström, K. Särkimäki, V. Bandaru, M.M. Skyllas, et al., Assessment of the runaway electron load distribution in ITER during 3D MHD induced beam termination, Plasma Phys. Control. Fusion 66 (2024), https://doi.org/10.1088/1361-6587/ad5fb5.